ORIGINAL PAPER

Dynamical analysis and applications of a novel 2-D hybrid dual-memristor hyperchaotic map with complexity enhancement

Shaohua Zhang · Hongli Zhang · Cong Wang

Abstract The dual-memristor hyperchaotic map has not yet received much attention and application, and its complexity and flexibility deserve further improvement. To this end, a novel two-dimensional hybrid dual-memristor (HDM) hyperchaotic map with complexity enhancement is constructed by connecting two different discrete memristors through self-feedback and sinusoidal transformation. The considered map has line invariant points related to the initial conditions of the discrete memristor, and it is Lyapunov stable or unstable. Taking the coupling strengths, memristor parameters, and initial conditions as tunable parameters, complex dynamical behaviors are investigated by numerical methods, including special bifurcation modes, a plethora of strange attractors, hyperchaotic attractors, and multi-stability behaviors. In particular, the performance evaluation of strange attractors with different topological structures is performed, and the complexity enhancement characteristic of the hyperchaotic attractor is confirmed by excellent dynamical performance indicators. In addition, without affecting the dynamical performance, the flexibility of the HDM map is effectively improved by switching control. Afterward, the pseudo-random number generator and image encryption strategy are proposed based on the hyperchaotic sequences

generated by the HDM map to improve its practical application value. The proposed encryption strategy fully utilizes the high randomness, complexity, and flexibility of the hyperchaotic sequences, exhibiting remarkable applicability and robustness in encrypting both typical color and non-typical grayscale images. Comprehensive analyses, including histogram, correlation, and information entropy analyses, as well as differential, data loss, and noise attacks, are conducted to thoroughly evaluate the performance of the encryption strategy. The results indicate that the strategy achieves superior encryption effectiveness and high security. Finally, a microcontroller-based digital circuit experiment platform is developed for verifying the numerical results.

1 Introduction

As a nonlinear circuit element that describes the relationship between charge and magnetic flux, the memristor has promoted the development of various fields since it was proposed and manufactured [1, 2], such as nonlinear systems, neuromorphic computing, secure communication, and prediction classification [3–6]. In particular, because of the inherent internal

S. Zhang · H. Zhang (✉) · C. Wang
School of Electrical Engineering, Xinjiang University,
Urumqi 830017, Xinjiang, China
e-mail: zhl@xju.edu.cn

state variables and excellent nonlinear characteristics, memristors instead of traditional nonlinear terms to construct nonlinear systems not only conform to the practical physical significance but also can induce more abundant dynamical behaviors [7, 8]. Specifically, utilizing nonlinear memristors to simulate the electromagnetic radiation and the neural synapse, Lin et al. [9, 10] proposed five-dimensional and eight-dimensional memristive Hopfield neural network models, which exhibit complex hyperchaotic behaviors. Then, the performance of hyperchaotic sequences was verified through image encryption experiments. Moreover, Ding et al. [11] investigated the chaotic dynamics and multi-stability phenomena of a six-dimensional memristive coupled tabu learning neuron model with electromagnetic radiation, and the randomness of the model was tested in voice encryption. However, high-dimensional models of memristive systems require expensive and complex computational resources, and the resulting hyperchaotic and chaotic behaviors often exhibit relatively low complexity. Especially when implementing these behaviors on some finite precision devices, the influence of noise and measurement errors can lead to degradation phenomena in low-complexity chaos [12–14], directly affecting the performance and application effects of these nonlinear systems. On the other hand, using diverse prediction techniques such as echo state networks [15], long short-term memory neural networks [16], and temporal convolutional networks [17] can accurately reproduce the evolution process of these chaotic or hyperchaotic sequences. However, this does not completely guarantee the security of chaos-based image encryption and secure communication, nor the effectiveness in chaos-based signal detection. Therefore, implementing high-complexity hyperchaotic phenomena with low-dimensional models is crucial for extending the wide application of memristive systems or maps and is also the main motivation behind this paper. Compared with continuous memristors, discrete memristors are promising to solve these significant challenges mentioned above because the discrete memristive map can produce more complex chaotic or hyperchaotic behaviors in the case of lower dimensions and has higher computational efficiency [18, 19]. Therefore, it is valuable and exciting work to construct the novel discrete memristor map and enhance the complexity of dynamical behavior.

For the above purpose, the tremendous ideal discrete memristors are proposed [20, 21], which show complex nonlinear characteristics and are also consistent with the three essential feature fingerprints of the memristor [22]. Significantly, the memristive hyperchaotic map increases the complexity of the dynamical behavior to a certain extent and produces diversified applications. It is worth noting that the memristive mapping model can generate complex hyperchaotic attractors in only two dimensions, while the continuous-time system requires at least four dimensions. Specifically, Bao et al. [23] improved the complexity of the traditional Logistic map by introducing a discrete memristor model, which shows critical stability and hyperchaotic behaviors. Lai et al. [24] constructed a two-dimensional (2-D) memristive Gaussian mapping model based on a sinusoidal memristor and generated hidden hyperchaotic attractors. Of course, the hyperchaotic attractors were also found in 2-D memristive Lozi, Hénon, and Tent maps, which have high randomness [5, 25–28]. Among them, a general 2-D memristive mapping model based on a cosinusoidal memristor was proposed in [5], which could enhance complexity and also achieve amplitude-controlled characteristics. In particular, there are also relevant reports on enhancing the complexity of maps utilizing nonlinear transformation [29–31], in which the map based on sinusoidal and logarithmic transformation can show more complex dynamical behavior. To our knowledge, the above memristive maps are generated by coupling a discrete memristor and a traditional map. In a nutshell, whether the map composed of only discrete memristors has excellent dynamical performance and how to enhance its complexity is a problem worthy of further consideration and a new research hotspot.

Very recently, the universal 2-D single-memristor hyperchaotic map was proposed in [32], and the hyperchaotic behaviors and coexisting multi-stability phenomena were found in four specific maps. Based on [32], by introducing two identical discrete memristors, a 3-D parallel dual-memristor hyperchaotic map was constructed in [33], and the extreme multistability related to the initial conditions was studied. Similarly, some high-dimensional memristive mapping models were proposed by cascade, parallel, and composite operations and applied to pseudo-random number generators (PRNGs) in [34]. Although the memristive maps presented in [33, 34] can produce

hyperchaotic behaviors, the dimension is higher and does not show the novel amplitude-controlled and offset-boosted dynamical behaviors described in [5, 29, 32, 35], that is, the flexibility is low. It can also be found that these maps rarely consider the coupling between two different types of discrete memristors, and the hyperchaotic dynamical behavior has not been enhanced and applied in image encryption. In general, it is significant to develop hyperchaotic maps with simple algebraic structures by composing different discrete memristors. Similarly, enhancing the complexity and flexibility of these maps will make outstanding contributions to improving the practical value of engineering applications based on hyperchaos.

Driven by the problems mentioned above, a novel 2-D hybrid dual-memristor (HDM) hyperchaotic map with excellent complexity is proposed in this paper, which connects two different discrete memristors in parallel through self-feedback and sinusoidal transformation as in [31]. The innovation and main contributions of this paper are summarized as follows. (1) A novel 2-D HDM hyperchaotic mapping model with line invariant points is proposed, which is very different from the model in [33]. The highlight is that the mapping model takes into account two different discrete memristors and can enrich the dynamical behavior and enhance the complexity. (2) The complicated bifurcation mechanisms and the coexisting multi-stability of the HDM map are analyzed, and the strange attractors with different topological structures induced by parameters are disclosed. The comparison results of dynamical performance show that the hyperchaotic sequences generated by the considered map have excellent complexity enhancement characteristics, and the PRNG test results also confirm that the sequence has high randomness. (3) The switching control strategy of the HDM map is investigated, which realizes the amplitude-controlled and offset-boosted characteristics of the hyperchaotic sequences, and proves the application value of the map in image encryption experiments.

The research is divided into three parts: modeling, dynamical analysis, and two applications, as shown in the schematic diagram in Fig. 1. Specifically, Part 1 presents the modeling process, which explains the structure of the proposed HDM map with complexity enhancement. In Part 2, the dynamical analysis is introduced, including the detailed steps of stability analysis, numerical simulation, evaluation of complexity enhancement, and digital circuit experimental verification. Furthermore, the applications of hyperchaotic sequences in PRNG and image encryption are paid more attention to in Part 3.

The remainder of the paper is arranged as follows. In Sect. 2, a novel 2-D HDM hyperchaotic map is proposed by combining two different memristors and sinusoidal transformation. In Sect. 3, numerical simulations reveal the bifurcation mechanism, strange attractor behavior, and coexisting multi-stability of the HDM map. In Sect. 4, the complexity enhancement characteristic of the HDM map is proved, the PRNGs are designed, and the digital circuit implementation experiments are performed. In Sect. 5, the flexible switching control for hyperchaotic sequences is investigated and applied to image encryption. Finally, Sect. 6 concludes the paper.

2 The 2-D hybrid dual-memristor hyperchaotic mapping model

This section proposes a 2-D HDM hyperchaotic mapping strategy based on sinusoidal transformation and establishes its simplified mathematical model. At the same time, we analyze in detail the stability of the invariant points that depend on parameters and initial conditions.

2.1 Description of discrete memristor

Due to the unique nonlinearity and iterative mechanism, discrete memristors play an essential role in constructing hyperchaotic maps. The continuous memristor can be converted into a discrete memristor by the forward Euler method [20] and the backward differential theory [21]. Therefore, an ideal charge-controlled discrete memristor model can be described by

$$\begin{cases} v_n = M(q_n)i_n, \\ q_{n+1} = i_n + hq_n, \end{cases} \tag{1}$$

where v_n, i_n, and q_n are the n-th iteration values of voltage $v(t)$, current $i(t)$, and charge $q(t)$ in the continuous memristor; q_{n+1} is the $(n + 1)$-th iteration value and h represents the iteration step size, usually set to 1. Specifically, since the 2-D HDM hyperchaotic
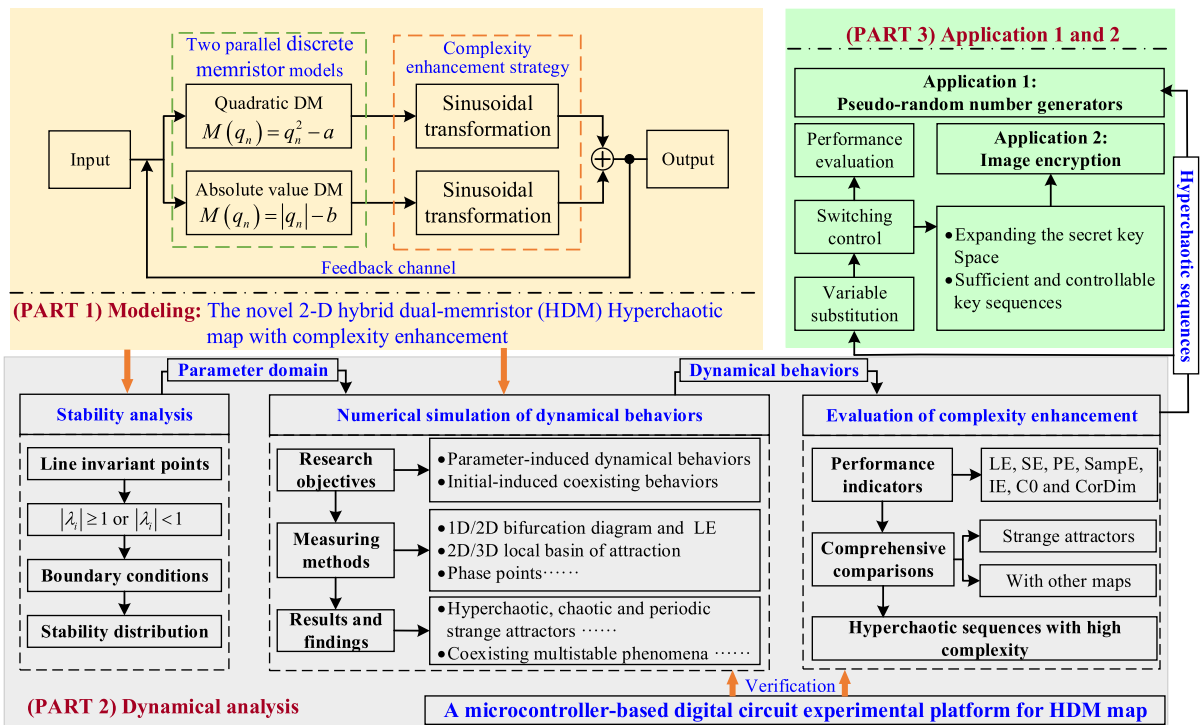
Fig. 1 Schematic diagram of the research in this paper

map has different discrete memristor models, according to [32], two types of DM models can be established by

$$\begin{cases} v_n = (q_n^2 - a)i_n, \\ q_{n+1} = i_n + q_n, \end{cases} \tag{2}$$

and

$$\begin{cases} v_n = (|q_n| - b)i_n, \\ q_{n+1} = i_n + q_n, \end{cases} \tag{3}$$

wherein the model described in Eq. (2) is called a quadratic discrete memristor (QDM), while Eq. (3) represents an absolute discrete memristor (ADM). As can be seen from Eqs. (2) and (3), the quadratic and absolute functions represent the nonlinear characteristics of discrete memristors, and the change of their internal state q_n makes them have a special memory effect. To demonstrate the essential characteristic fingerprints of the two discrete memristors, $a = b = 1$ is fixed, and the discrete bipolar periodic signal $I = 0.1 \sin(\omega n)$ A is chosen as the current excitation, where ω is the angular frequency (rad/s) and n represents the n-th iteration. When the initial condition of two discrete memristors is $q_0 = 0$ C, the output

characteristics on the $i_n - v_n$ plane present a hysteresis loop across the origin and the lobe area shown in Fig. 2a and c gradually decreases as ω increases.
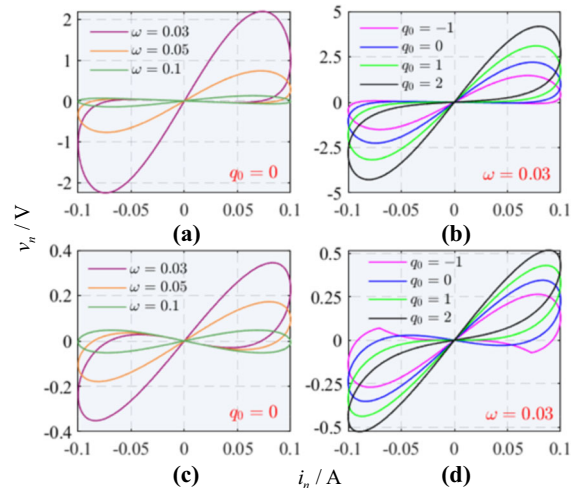

Fig. 2 Pinch hysteresis loops of two discrete memristors with $I = 0.1 \sin(\omega n)$ A. **a** Characteristics of QDM varying with ω for $q_0 = 0$ C. **b** Multi-stable characteristics of QDM varying with q_0 for $\omega = 0.03$ rad/s. **c** Characteristics of ADM varying with ω for $q_0 = 0$ C. **d** Multi-stable characteristics of ADM varying with q_0 for $\omega = 0.03$ rad/s

Surprisingly, when ω is set to 0.03 rad/s, multiple types of pinch hysteresis loops induced by different initial conditions are shown in Fig. 2b and d, which also confirm that the two discrete memristors are multi-stable.

2.2 Complexity enhancement strategy and mathematical model of HDM map

To enhance the complexity of the existing dual-memristor maps, a general complexity enhancement strategy based on sinusoidal transformation is proposed, and a novel HDM hyperchaotic mapping model containing two different discrete memristors is constructed. Inspired by [31], the general novel complexity enhancement structure of the dual-memristor map is shown in Fig. 3.

In Fig. 3, two different charge-controlled discrete memristors are coupled in parallel and have the same input x_n. Significantly, the memristance $M_1(q_n)$ and $M_2(q_n)$ are enhanced by the sinusoidal transformation, which makes the model and the generated hyperchaotic sequence more complex. Then, the enhanced signal is converted into the output iteration value x_{n+1} by the sum function, which is fed back to the input port to perform the next iteration. Therefore, according to Fig. 3, a general novel HDM hyperchaotic mapping model with complexity enhancement can be modeled by

$$\begin{cases} x_{n+1} = k_1 \sin(M_1(q_n)x_n) + k_2 \sin(M_2(q_n)x_n), \\ q_{n+1} = x_n + q_n, \end{cases} \quad (4)$$

where k_1 and k_2 are the coupled coefficients. In fact, the HDM mapping model should be three-dimensional, but because the change of charge q_n in the ideal discrete memristors is described by the same algebraic structure as shown in Eqs. (2) and (3), to make the model simpler and improve computational efficiency,
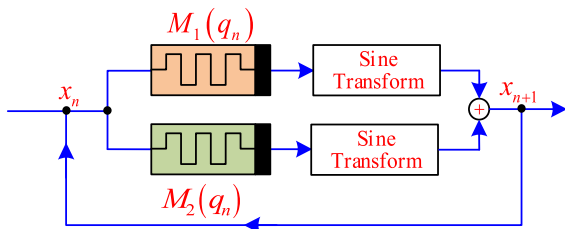
Eq. (4) considers that the change of charge q_n is the same, which can also exhibit intricate dynamical behaviors. It is worth explaining that the HDM mapping model is suitable for coupling any two types of discrete memristors.

After substituting QDM and ADM represented by Eqs. (2) and (3) into Eq. (4), respectively, a specific HDM mapping model can be derived as

$$\begin{cases} x_{n+1} = k_1 \sin((q_n^2 - a)x_n) + k_2 \sin((|q_n| - b)x_n), \\ q_{n+1} = x_n + q_n. \end{cases} \quad (5)$$

When Eq. (5) is modulated by coupling strengths (k_1 and k_2) and memristor parameters (a and b), it can exhibit abundant dynamical behaviors and generate more complex hyperchaos sequences.

2.3 Line invariant point and its stability analysis

For nonlinear discrete maps, the linear analysis method based on small perturbation is often used to explore the stability of invariant points. Assume that the invariant point of the HDM mapping model (5) is $S = (x_{eq}, q_{eq})$ and when small perturbations $\Delta x_n = x_n - x_{eq}$ and $\Delta q_n = q_n - q_{eq}$ are added to S, respectively, Eq. (5) can be converted into

$$\begin{cases} x_{eq} + \Delta x_{n+1} = F_1(x_{eq} + \Delta x_n, q_{eq} + \Delta q_n), \\ q_{eq} + \Delta q_{n+1} = F_2(x_{eq} + \Delta x_n, q_{eq} + \Delta q_n), \end{cases} \quad (6)$$

where $F_1(\cdot)$ and $F_2(\cdot)$ are the right-hand expressions of Eq. (5). When the trajectory is zoomed into an infinitely small area near S, the nonlinear interaction can be ignored, and Eq. (6) can be approximated linearly by

$$\begin{bmatrix} x_{eq} + \Delta x_{n+1} \\ q_{eq} + \Delta q_{n+1} \end{bmatrix} \approx \begin{bmatrix} F_1(x_{eq}) \\ F_2(q_{eq}) \end{bmatrix} + \begin{bmatrix} \dfrac{\partial F_1}{\partial x_n} & \dfrac{\partial F_1}{\partial q_n} \\ \dfrac{\partial F_2}{\partial x_n} & \dfrac{\partial F_2}{\partial q_n} \end{bmatrix} \Bigg|_{\substack{x_n = x_{eq} \\ q_n = q_{eq}}} \begin{bmatrix} \Delta x_n \\ \Delta q_n \end{bmatrix}. \quad (7)$$

Because $x_{eq} = F_1(x_{eq})$ and $q_{eq} = F_2(q_{eq})$, Eq. (7) is equivalent to

Fig. 3 General novel complexity enhancement structure of the dual-memristor map

$$\begin{bmatrix} \Delta x_{n+1} \\ \Delta q_{n+1} \end{bmatrix} \approx J_S \begin{bmatrix} \Delta x_n \\ \Delta q_n \end{bmatrix}$$

$$= \begin{bmatrix} \dfrac{\partial F_1}{\partial x_n} & \dfrac{\partial F_1}{\partial q_n} \\ \dfrac{\partial F_2}{\partial x_n} & \dfrac{\partial F_2}{\partial q_n} \end{bmatrix}\Bigg|_{\substack{x_n=x_{eq} \\ q_n=q_{eq}}} \begin{bmatrix} \Delta x_n \\ \Delta q_n \end{bmatrix}, \qquad (8)$$

where J_S is the Jacobian matrix of S. Therefore, the stability of the HDM map is related to small perturbations and can be judged by the eigenvalues of the characteristic equation of J_S. Specifically, $S = (0, \eta)$ can be calculated from Eq. (5), which indicates that the HDM map has an infinite number of line invariant points. Meanwhile, the expression of J_S at $S = (0, \eta)$ can also be obtained by

$$J_S = \begin{bmatrix} k_1(\eta^2 - a) + k_2(|\eta| - b) & 1 \\ 1 & 1 \end{bmatrix}. \qquad (9)$$

The corresponding characteristic polynomial can be derived as

$$\det(\lambda I - J_S) = (\lambda - 1)\big(\lambda - \big(k_1\big(\eta^2 - a\big) + k_2(|\eta| - b)\big)\big). \qquad (10)$$

Therefore, the eigenvalue of J_S can be solved as

$$\lambda_1 = 1, \quad \lambda_2 = k_1\big(\eta^2 - a\big) + k_2(|\eta| - b). \qquad (11)$$

According to the stability theory of discrete systems [36], since $|\lambda_1| = 1$ is constant, S can only be unstable ($|\lambda_2| > 1$) and Lyapunov stable ($|\lambda_2| \le 1$), that is, critically stable. For initial condition-dependent stability, because η in Eq. (11) is separable, the stability region of S can be determined by η, and it should be noted that the parameters used for analysis are greater than 0. Let $\Delta_1 = k_2^2 + 4k_1(ak_1 + bk_2 + 1)$ and $\Delta_2 = k_2^2 + 4k_1(ak_1 + bk_2 - 1)$, when S is Lyapunov stable, η need to meet

$$\begin{cases} \eta \in \left[\dfrac{k_2 - \sqrt{\Delta_1}}{2k_1} \ \dfrac{-k_2 + \sqrt{\Delta_1}}{2k_1}\right], \text{for } ak_1 + bk_2 \le 1 \\ \eta \in \left[\dfrac{k_2 - \sqrt{\Delta_1}}{2k_1} \ \dfrac{k_2 - \sqrt{\Delta_2}}{2k_1}\right] \cup \left[\dfrac{-k_2 + \sqrt{\Delta_2}}{2k_1} \ \dfrac{-k_2 + \sqrt{\Delta_1}}{2k_1}\right]. \text{for } ak_1 + bk_2 > 1 \end{cases}$$

$$(12)$$

Otherwise, S is unstable.

For parameters-dependent stability, when $\eta = 0.1$, $a = 1$, and $b = 1$ are fixed, $|\lambda_2|$ corresponding to each parameter set (k_1, k_2) can be calculated according to Eq. (11) by setting $k_1 \in [1 : 0.005:2.5]$ and

$k_2 \in [-1 : 0.005:1]$. Therefore, the stability distribution of S related to coupling strengths is shown in Fig. 4a, where the Lyapunov stable region presents a triangular shape filled with dark gray, and the yellow region represents the unstable. Similarly, When $k_1 = 1.5$ and $k_2 = 0.8$ are fixed, $|\lambda_2|$ corresponding to (a, b) can also be obtained with $a \in [-5 : 0.02 : 5]$ and $b \in [0 : 0.02:10]$. Figure 4b shows the stable distribution of S related to memristor parameters on the 2-D parameter plane and has a tilted Lyapunov stable region. As we can see, the cyan dotted line in Fig. 4 represents the boundary condition calculated by Eq. (11), which can clearly distinguish the Lyapunov stable region from the unstable region.

In summary, the stability of the HDM mapping model (5) can be controlled by coupling strengths, memristor parameters, and initial conditions, resulting in complex dynamical behaviors in the unstable region.

3 Dynamical analysis by numerical methods

Based on the stability analysis, this section studies the coupling strength-induced and memristor parameter-induced bifurcation mechanisms, as well as the coexisting multi-stability induced by initial conditions. Various strange chaotic/hyperchaotic attractors are excavated through dynamical analysis techniques, which have high complexity. In addition, the numerical simulations are performed in MATLAB, and the total number of iterations is 25,000. To eliminate the transient effect of the state trajectories, the first 10,000 data points are discarded.

3.1 Parameter-induced complex dynamical behaviors

To distinguish various dynamical behaviors in the HDM map, the relevant bifurcation parameters are mapped to the 2-D parameter space, and the 2-D bifurcation diagram filled with different colors can be obtained by calculating the period number of the corresponding state trajectories for each set of parameters. In addition, the 2-D Lyapunov exponent (LE) spectrum can be used to confirm different dynamical behavior distributions depicted by the 2-D bifurcation diagram.
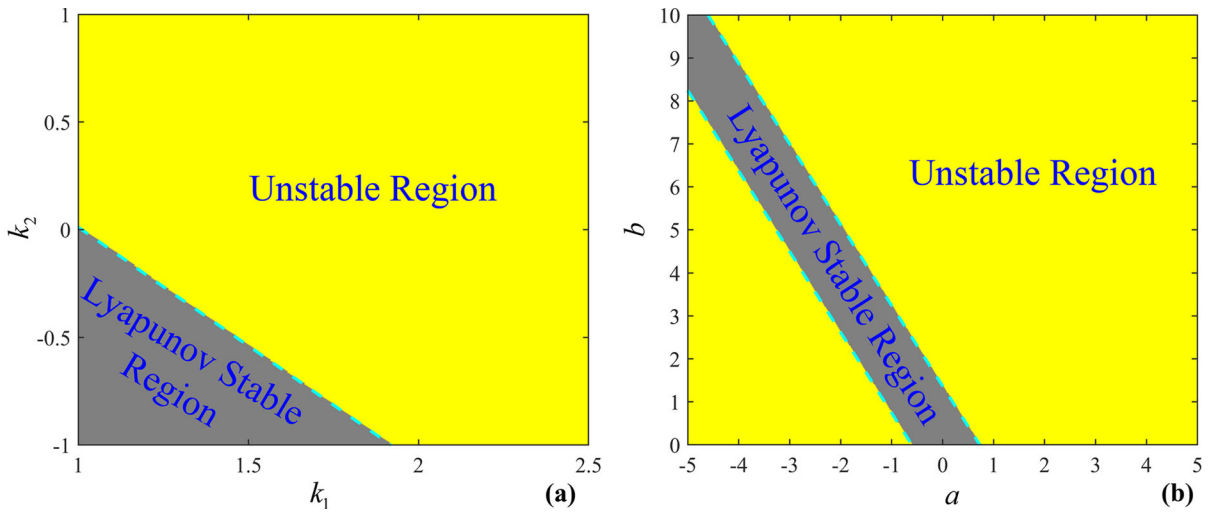
Fig. 4 Stability distribution diagram of S on 2-D parameter plane for $\eta = 0.1$. **a** Stability of S related to coupling strengths (k_1 and k_2) for $a = 1$ and $b = 1$; **b** Stability of S related to memristor parameters (a and b) for $k_1 = 1.5$ and $k_2 = 0.8$

Specifically, when the memristor parameters are set to $(a, b) = (1, 1)$, the coupling strength-induced 2-D bifurcation diagram and LE spectrum on the $k_1 - k_2$ plane are given, as shown in Fig. 5, where $k_1 \in [1, 2.5]$ and $k_2 \in [-1, 1]$. It is worth mentioning that the LE of the HDM map is calculated using the QR decomposition method [37] for each set of bifurcation parameter adjustments. The identification of chaotic and hyperchaotic behaviors is accomplished by accurately counting the number of positive LEs. Specifically, chaos is characterized by one positive LE while hyperchaos requires at least two positive LEs. Moreover, if all LEs are non-positive, the resulting dynamical behaviors are classified as periodic and further distinguished into different periods based on the cycle number of peaks. For Fig. 5a, the hyperchaos (HC) with two positive LEs is filled with red, the chaos (CH) with one positive LE and one negative LE is filled with yellow, and the quasi-period (QP) with a zero LE is filled with magenta. In addition, for periodic oscillations with two negative LEs, the stable point (SP), the period-2 to period-8 (P02, P04, P06, and P08), and the
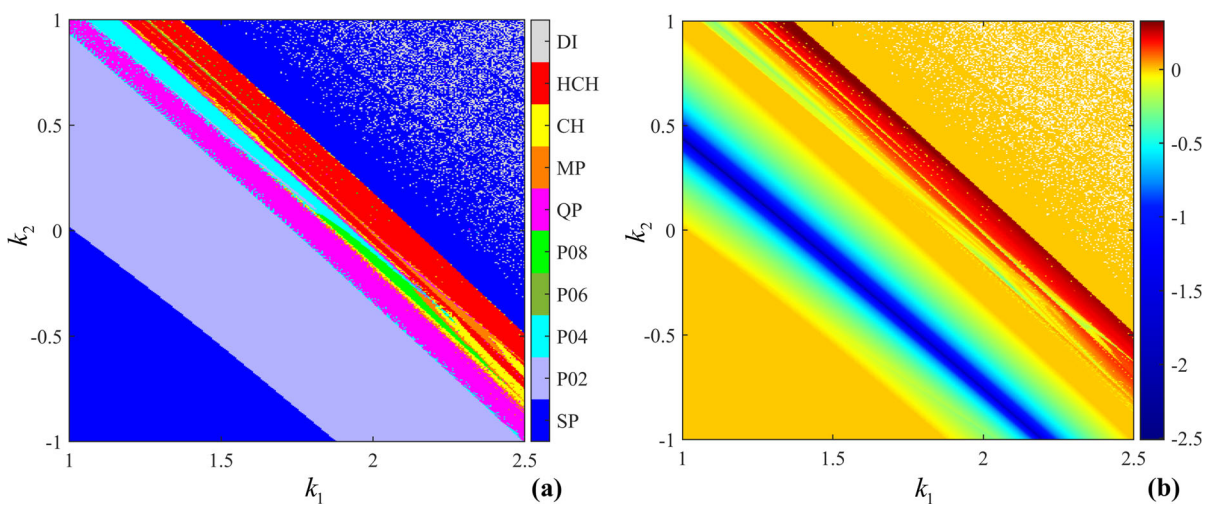

Fig. 5 For $(x_0, q_0) = (0.1, 0.1)$ and $(a, b) = (1, 1)$, the coupling strength-induced dynamical behaviors on the $k_1 - k_2$ plane with $k_1 \in [1, 2.5]$ and $k_2 \in [-1, 1]$. **a** 2-D bifurcation diagram; **b** 2-D LE spectrum

multi-period (MP) attractors are marked by other colors, respectively. Of course, the divergence behaviors (DI) are represented by light gray. For the 2-D LE spectrum shown in Fig. 5b, the greater the LE value of the state x_n, the darker the color, and the LE spectrum corresponds precisely to the dynamical behaviors depicted in Fig. 5a.

For $(k_1, k_2) = (1.5, 0.8)$, the memristor parameter-induced bifurcation behaviors are visualized in Fig. 6, where $a \in [-5, 5]$ and $b \in [0, 10]$. Similarly, ten dynamical behaviors appear in the 2-D bifurcation diagram shown in Fig. 6a and are labeled with the same colors as Fig. 6a. Of course, Fig. 6b indicates that the 2-D LE spectrum also accurately matches the 2-D bifurcation diagram. Figures 5 and 6 disclose that coupling strengths and memristor parameters can affect the HDM mapping model (5) to generate diverse dynamical behaviors. It should be noted that the stability distribution of Figs. 5 and 6 is slightly different from that of Fig. 4, which is caused by $|\lambda_1| = 1$ and further illustrates the diversified dynamical evolutions of the map.

3.2 Bifurcation mechanisms and strange attractor

The evolution process of different dynamical behaviors can be characterized in detail by the 1-D bifurcation diagram and LE spectrum controlled by the coupling strengths and memristor parameters, from which various strange attractors with different topological structures can be captured. For the sake of

convenience, the dynamical behaviors driven by k_1, k_2, a, and b are defined as **Case 1** with $(k_1, k_2, a, b) = (k_1, 0.1, 1, 1)$, **Case 2** with $(k_1, k_2, a, b) = (1, k_2, 1, 1)$, **Case 3** with $(k_1, k_2, a, b) = (1.5, 0.8, a, 4)$, and **Case 4** with $(k_1, k_2, a, b) = (1.5, 0.8, 0.2, b)$, respectively. Therefore, Fig. 7 reveals different bifurcation mechanisms of four cases, and Fig. 8 visualizes the typical strange attractors.

For Case 1, when the bifurcation interval of the control parameter k_1 is set to $k_1 \in [1.5, 2.1]$, the bifurcation diagram of the HDM map and the corresponding LEs are shown in Fig. 7a. As k_2 increases, the state trajectory (x, q) first switches from period-2 bifurcation for $k_1 \in [1.5, 1.65]$ to a quasi-periodic bifurcation with zero LE for $k_1 \in [1.65, 1.78]$, then from period-4 bifurcation for $k_1 \in [1.78, 1.87]$ to a hyperchaotic domain with two positive LEs for $k_1 \in [1.87, 2.05]$ via a narrower period-8 bifurcation, and finally degenerates into a stable point attractor. Meanwhile, the above-mentioned dynamical behaviors can be verified by comparing the bifurcation diagram at the top and LE at the bottom in Fig. 7a. In addition, several typical parameter-driven hyperchaotic ($k_1 = 2.05$ and $k_1 = 2$), period-4 ($k_1 = 1.85$), period-8 ($k_1 = 1.8$), and quasi-periodic ($k_1 = 1.7$) attractors with different topological structures are visualized by the phase diagram in Fig. 8a1–a5.

For Case 2, when the bifurcation parameter k_2 is set to $k_2 \in [0.6, 1.5]$, the bifurcation diagram and LE spectrum varying with k_2 are shown at the top and
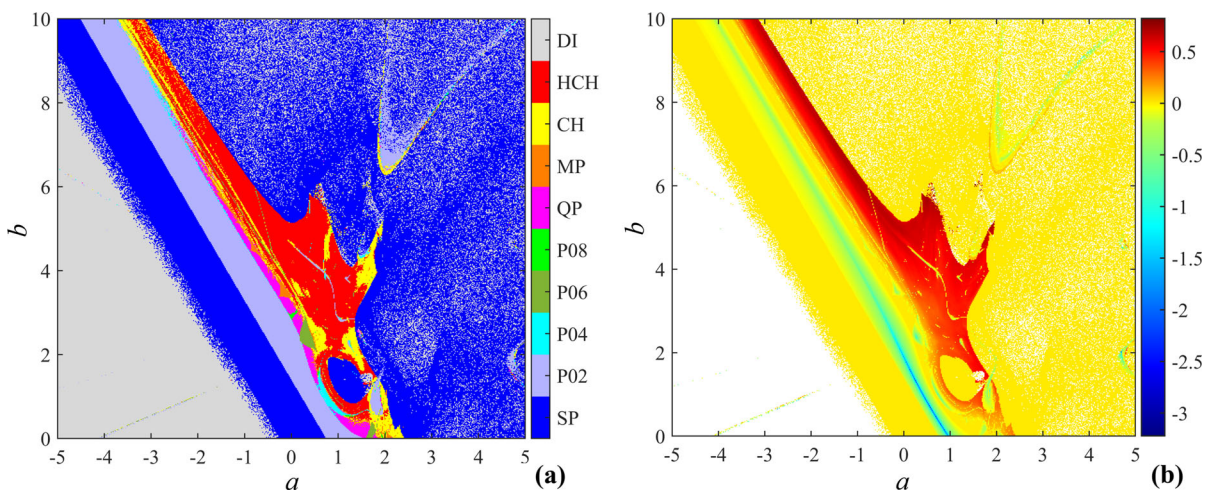

Fig. 6 For $(x_0, q_0) = (0.1, 0.1)$ and $(k_1, k_2) = (1.5, 0.8)$, the memristor parameter-induced dynamical behaviors on the $a-b$ plane with $a \in [-5, 5]$ and $b \in [0, 10]$. **a** 2-D bifurcation diagram; **b** 2-D LE spectrum
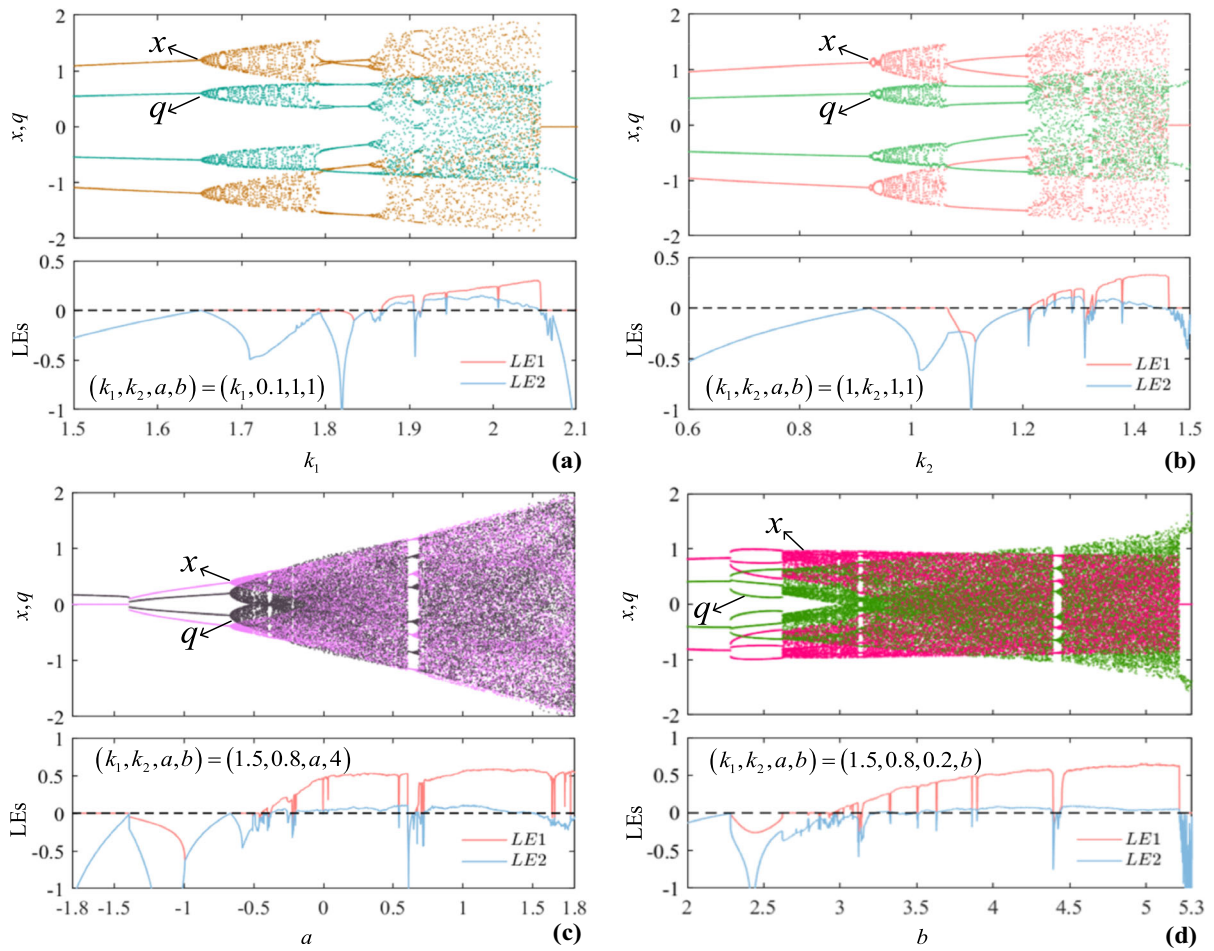
Fig. 7 1-D bifurcation diagram and LE spectrum corresponding to the four cases with $(x_0, q_0) = (0.1, 0.1)$. **a** Case 1 with $(k_1, k_2, a, b) = (k_1, 0.1, 1, 1)$; **b** Case 2 with $(k_1, k_2, a, b) = (1, k_2, 1, 1)$; **c** Case 3 with $(k_1, k_2, a, b) = (1.5, 0.8, a, 4)$; **d** Case 4 with $(k_1, k_2, a, b) = (1.5, 0.8, 0.2, b)$

bottom of Fig. 7b. It can be seen from Fig. 7b that the trajectory transits from period-2 to quasi-periodic bifurcation at $k_2 = 0.92$ and enters period-4 bifurcation at $k_2 = 1.07$. Furthermore, the considered map also contains a small chaotic domain for $k_2 \in [1.21, 1.23]$, and the hyperchaotic domain with a narrow periodic window is located in $k_2 \in [1.23, 1.31] \cup [1.33, 1.44]$. Meanwhile, typical strange attractors with different shapes representing different bifurcation stages are also measured from Fig. 8b1–b5.

For Case 3, as the memristor parameter a increases in $a \in [-1.8, 1.8]$, it can be seen that when $a \in [-0.44, -0.2] \cup [1.51, 1.8]$ and $a \in [-0.2, 0.6] \cup$

$[0.66, 1.51]$, the HDM map can generate more complex chaotic and hyperchaotic behaviors in an extensive range, respectively, and their first LE value is larger than the first two cases, as shown in Fig. 7c. Of course, various periodic behaviors are distributed in $a \in [-1.8, -0.44] \cup [0.6, 0.66]$. According to Fig. 7c, several strange attractors induced by a are shown in Fig. 8c1–c5, such as spiral hyperchaotic ($a = 1.2$), period-5 ($a = 0.7$), and symmetric chaotic attractors ($a = -0.2$) with two segments.

For Case 4, Fig. 7d shows the bifurcation diagram and LE spectrum related to the memristor parameter b with $b \in [2, 5.3]$. When $b \in [3.24, 3.36] \cup [3.51, 4.38] \cup [4.44, 5.21]$, the HDM map is leading
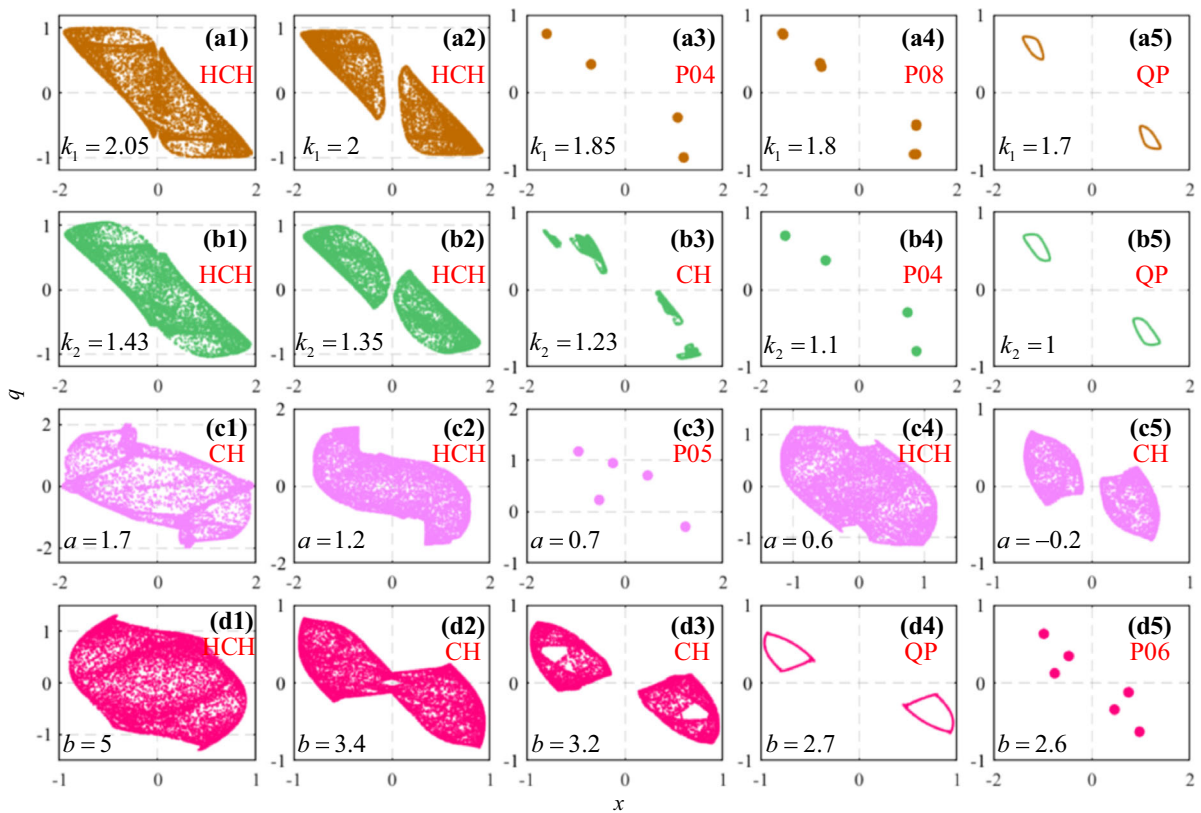
Fig. 8 Visualization of strange attractors with different topologies for $(x_0, q_0) = (0.1, 0.1)$. **a** Case 1 with $k_1 = 2.05, 2, 1.85, 1.8,$ and $1.7;$ **b** Case 2 with $k_2 = 1.43, 1.35, 1.23, 1.1,$ and $1;$ $a = 1.7, 1.2, 0.7, 0.6,$ and $-0.2;$ **c** Case 3 with $b = 5, 3.4, 3.2, 2.7,$ and 2.6 **d** Case 4 with

to hyperchaos because both LEs are positive, and chaos appears in $b \in [2.96, 3.24] \cup [3.36, 3.51]$ with only one positive LE. Unlike Case 3, with the change of b, period-6 behavior occurs for the first time and is located in $b \in [2.28, 2.62]$. Similarly, symmetric hyperchaotic ($b = 5$), chaotic with hollow ($b = 3.4$ and $b = 3.2$), quasi-periodic ($b = 2.7$), and period-6 ($b = 2.6$) attractors are depicted in Fig. 8d1–d5.

As a result, compared with Fig. 7, the HDM map has larger chaotic and hyperchaotic intervals driven by a and b, and the maximum LE exceeds 0.5, which is almost not achieved in the related memristive maps. At the same time, slight variations in parameters can induce complex bifurcation behaviors and strange attractors with different topologies, which also indicate that the control parameters affect the HDM map to generate abundant dynamical behaviors, as shown in Fig. 8.

3.3 Local basin of attraction and coexisting multi-stability

Another novel dynamical behavior is coexisting multi-stability that can be reflected by the local basin of attraction induced by the initial conditions. Since the Lyapunov stable and unstable regions of the HDM map.are related to the initial condition q_0 according to Eqs. (11) and (12), the 3-D local basins of attraction labeled can be obtained by calculating the periodic number and LEs for four cases, as shown in Fig. 9. Then, the initial conditions ($x_0 \in [-2, 2]$ and $q_0 \in [-2, 2]$) are taken as the x-axis and y-axis, while the parameters ($k_1 \in [1.7, 2]$ for Case 1, $k_2 \in [1.2, 1.5]$ for Case 2, $a \in [-0.5, 1.5]$ for Case 3, and $b \in [3, 5]$ for Case 4) represent the z-axis. From the z-axis direction in Fig. 9, the color distribution intervals are approximately consistent with the dynamical behavior distribution intervals of four cases depicted in Fig. 7, so the HDM map has strong robustness to changes in
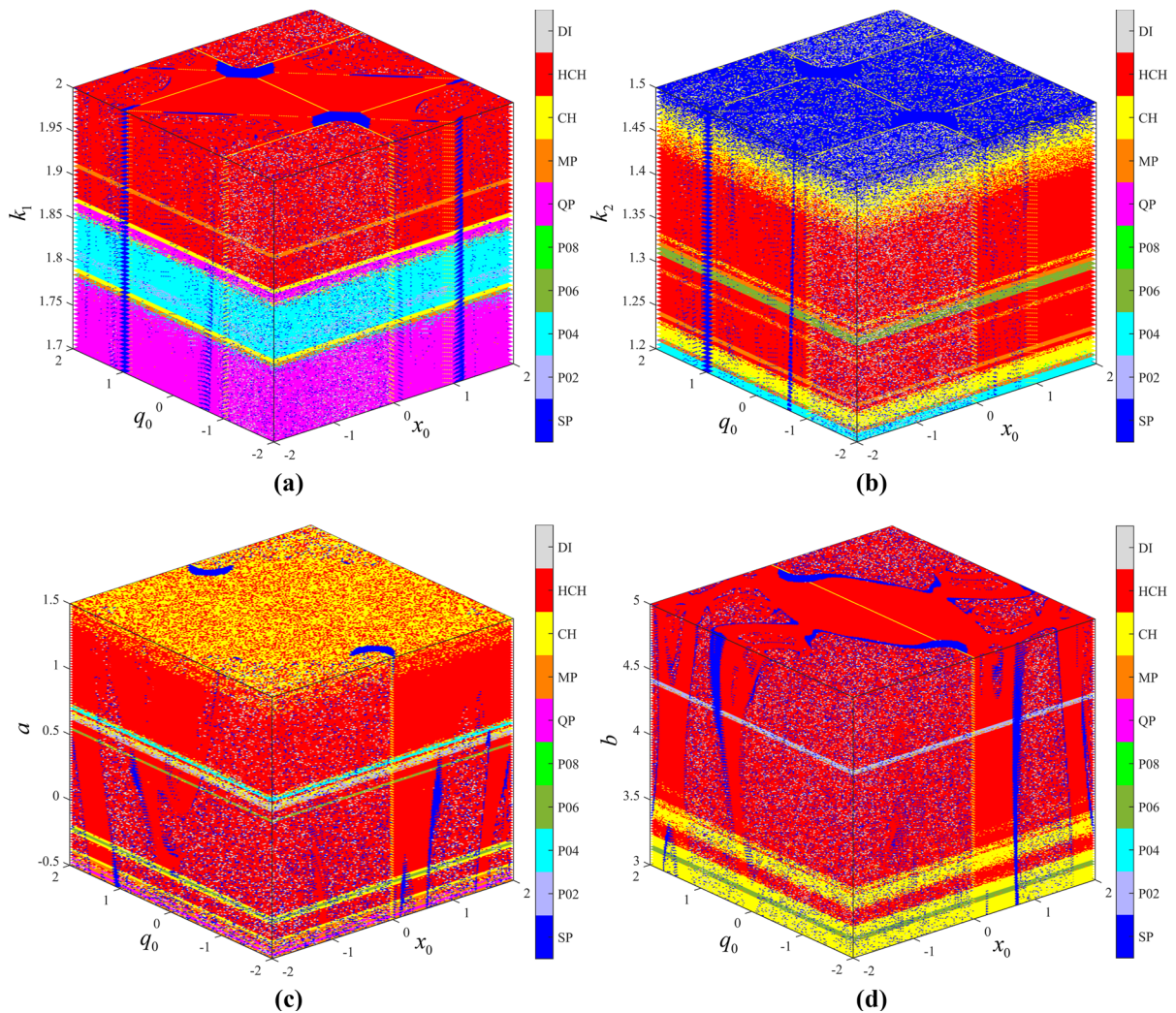
Fig. 9 3-D local basins of attractor for four cases with $x_0 \in [-2, 2]$ and $q_0 \in [-2, 2]$. **a** $k_1 \in [1.7, 2]$ for Case 1 on the $x_0 - q_0 - k_1$ plane; **b** $k_2 \in [1.2, 1.5]$ for Case 2 on the $x_0 - q_0 - k_2$ plane; **c** $a \in [-0.5, 1.5]$ for Case 3 on the $x_0 - q_0 - a$ plane; **d** $b \in [3, 5]$ for Case 4 on the $x_0 - q_0 - b$ plane

initial conditions. However, the $x_0 - q_0$ planes of Fig. 9 corresponding to each k_1, k_2, a, and b show different dynamical distributions, that is, the significantly different basins of attraction, indicating that the HDM map is multi-stable.

To reveal the essence of coexisting multi-stability and the robust performance of hyperchaotic/chaotic sequences, considering Case 4 as a representative, two central symmetric local basins of attraction are shown in Fig. 10 by selecting two sections in Fig. 9d. When $b = 5$ is fixed for Case 4, Fig. 10a shows the coexisting bi-stability of periodic points marked in blue and hyperchaotic behaviors marked in red on the

$x_0 - q_0$ plane. However, for $b = 3.4$, the bi-stability phenomenon in Fig. 10b is different from that of $b = 5$, because the HDM map exhibits yellow-labeled chaos and periodic points. Since most regions on the $x_0 - q_0$ plane are attractive to hyperchaos and chaos and there is no unbounded phenomenon, the HDM map shows strong robustness and ergodicity for initial conditions.

Since Sect. 2.3 indicates theoretically that the stability of the HDM map depends on q_0, the bifurcation diagram driven by q_0 with $x_0 = 0.1$ is reflected in Fig. 11. The bifurcation interval of the point attractors in Fig. 11a is
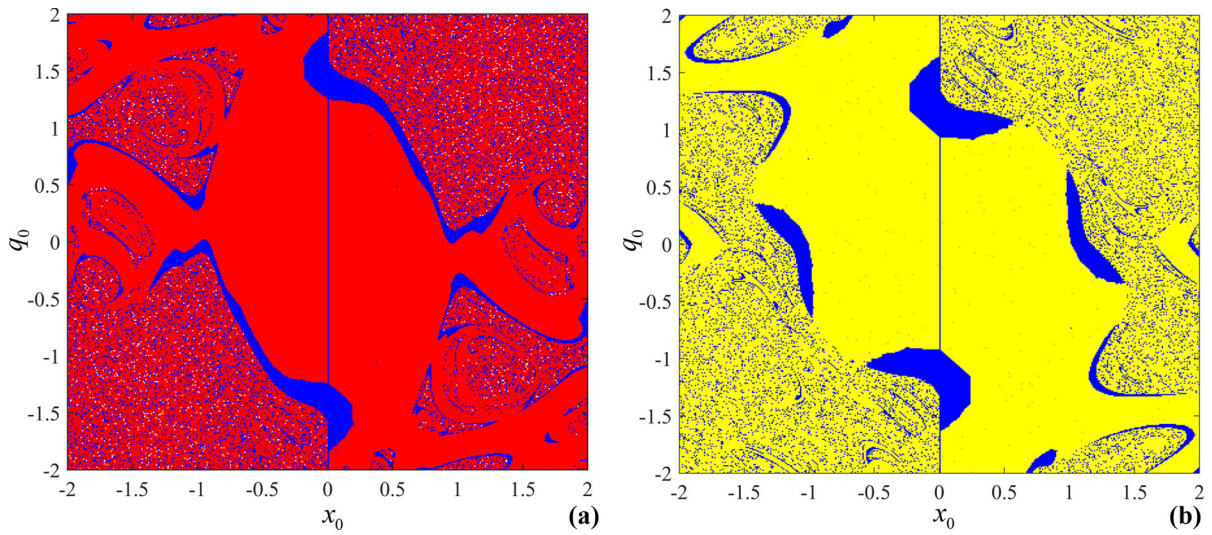
Fig. 10 2-D local basins of attractor for Case 4 with $x_0 \in [-2, 2]$ and $q_0 \in [-2, 2]$. **a** $b = 5$; **b** $b = 3.4$
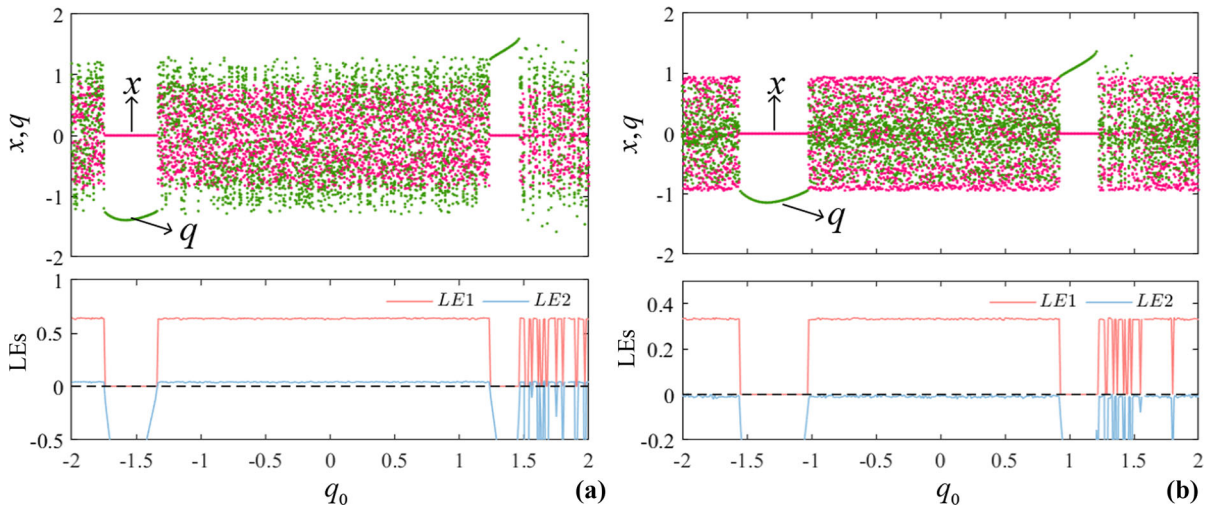

Fig. 11 Bifurcation diagram driven by q_0 with $x_0 = 0.1$. **a** $b = 5$; **b** $b = 3.4$

$q_0 \in [-1.75, -1.35] \cup [1.24, 1.46]$, and the remaining parameter domains represent hyperchaotic behavior with two positive LEs. In addition, when b changes to 3.4, the point attractors are distributed in $q_0 \in [-1.55, -1.03] \cup [0.93, 1.22]$, and the remaining parameter domains represent chaotic attractors with a positive LE, as shown in Fig. 11b. As depicted in Fig. 11, the bifurcation intervals occupied by chaos and hyperchaos are wide, and their LE values are uniformly distributed, proving the strong robustness of chaos and hyperchaos. However, the theoretically calculated Lyapunov stable domains are $q_0 \in$

$[-1.6319, -1.2404] \cup [1.2404, 1.6319]$ for $b = 5$ and $q_0 \in [-1.3920, -0.9240] \cup [0.9240, 1.3920]$ for $b = 3.4$, respectively, which are slightly different from the parameter domain of the stability point. The reason is also that the Lyapunov stability defined by $|\lambda_1| = 1$ is a critical stable state. The above analysis manifests that the HDM map has extremely complicated coexisting multi-stability phenomena, and the generated chaos and hyperchaos are robust to changes in initial conditions.

4 Complexity enhancement analysis and PRNG test

This section analyzes the complexity of strange attractors generated by the HDM map from a quantitative perspective, and the complexity enhancement performance of hyperchaotic sequences is comprehensively compared. In addition, pseudo-random number generators (PRNGs) are designed and tested to verify the high randomness of hyperchaotic sequences.

4.1 Dynamical performance analysis of strange attractors

It can be seen from Sect. 3.2 that the qualitative analysis reveals the complex evolution mechanism of strange attractors, but a variety of dynamical performance indicators can quantitatively measure the performance of attractors, which is the key to complexity analysis. Therefore, for the HDM map, comprehensive dynamical performance indicators of typical strange attractors in four cases, such as LE, spectral entropy (SE), permutation entropy (PE), sample entropy (SampE), information entropy (IE), C0 complexity (C0), and correlation dimension (CorDim), are calculated and summarized in Table 1. Please note that to obtain reliable conclusions, the iteration step size of the numerical simulation in this

section is set to 110,000, and the first 10,000 data points are discarded.

According to the analysis for Table 1, the hyperchaotic attractors induced by four parameters have two positive LEs, which are larger than those of chaotic and periodic attractors, indicating that the hyperchaotic sequences have more complicated characteristics. Meanwhile, the normalized SE shows that hyperchaotic attractors are more similar to random signals than chaotic and periodic attractors, especially 0.9333 and 0.9494 for $a = 1.2$ and $b = 5$, respectively. In particular, in the comparisons of PE, SampE, and C0, it can also be found that all the hyperchaotic attractors, especially when $a = 1.2$ in Case 3, have superior dynamical performance. However, IE values of hyperchaotic and chaotic attractors are closer to 8, representing more information, that is, the higher the uncertainty. Finally, by comparing the CorDim value, it can be concluded that the fractal characteristics of hyperchaotic/chaotic attractors are more complex than the periodic behaviors. Therefore, the greater the dynamical performance indicators of the strange attractors, the higher the randomness of the corresponding time series and the more complicated the oscillation form.

Although the four hyperchaotic attractors in Table 1 have excellent dynamical performance, their structures and iterative sequences are different, as shown in Fig. 12. Importantly, to test and verify that the

Table 1 Dynamical performance indicators of typical strange attractors in four cases

Cases	Parameters	Attractors	LE1, LE2	SE	PE	SampE	IE	C0	CorDim	Q
Case 1	**2**	**Hyperchaos**	**0.2369, 0.1252**	**0.9175**	**3.6687**	**1.0447**	**7.9838**	**0.1750**	**1.9313**	**2.0104**
	1.85	Period-4	$- 0.0066, - 0.0067$	0.1461	2.6325	0.4055	3.8611	0.0025	0.0000	0.8793
	1.7	Quasi-period	$0.0000, - 0.2440$	0.0048	2.6549	0.4175	7.9848	0.0001	1.0065	1.4781
Case 2	**1.43**	**Hyperchaos**	**0.3271, 0.0167**	**0.8337**	**3.5275**	**0.8615**	**7.9844**	**0.5622**	**1.7826**	**1.9870**
	1.23	Chaos	0.0679, -0.0021	0.2835	2.6125	0.2620	7.9861	0.0165	1.5920	1.6023
	1.1	Period-4	$- 0.2383, - 0.4827$	0.1461	1.3863	0.4055	2.0838	0.0024	0.0000	0.4129
Case 3	**1.2**	**Hyperchaos**	**0.5791, 0.0603**	**0.9333**	**5.3748**	**1.2147**	**7.9881**	**0.9738**	**2.6247**	**2.4686**
	0.7	Period-5	$- 0.0316, - 0.0316$	0.1544	2.2479	0.0000	2.8065	0.0096	0.0000	0.6444
	-0.2	Chaos	$0.2230, - 0.0127$	0.872	3.1394	0.6477	7.9865	0.1444	1.3648	1.7957
Case 4	**5**	**Hyperchaos**	**0.6369, 0.0372**	**0.9494**	**5.2512**	**1.2947**	**7.9858**	**0.9918**	**1.7348**	**2.3602**
	3.2	Chaos	0.1755, $- 0.0212$	0.8560	3.0793	0.7134	7.9852	0.1149	1.6377	1.8176
	2.6	Period-6	$- 0.1097, - 0.2635$	0.0000	1.7918	0.0000	1.8086	0.0000	0.0000	0.4034

The bold indicates that the dynamical performance of the hyperchaos is optimal in each case
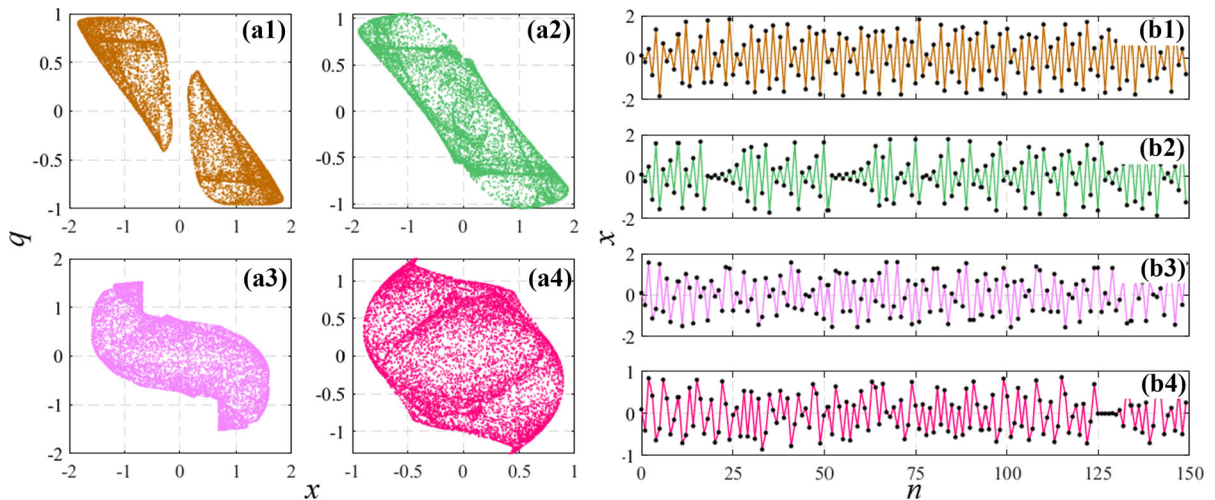
Fig. 12 Phase points and iterative sequences of hyperchaotic attractors generated by the HDM map for four cases. **(a1, b1)** $k_1 = 2$ for Case 1; **(a2, b2)** $k_2 = 1.43$ for Case 2; **(a3, b3)** $a = 1.2$ for Case 3; **(a4, b4)** $b = 5$ for Case 4

proposed map has complexity enhancement characteristics, it is necessary to evaluate the hyperchaotic attractors comprehensively. Therefore, the average value of the eight performance indicators is defined as Q and described by

$$Q = \frac{\text{LE1} + \text{LE2} + \text{SE} + \text{PE} + \text{SampE} + \text{IE} + \text{C0} + \text{CorDim}}{8}.$$
(13)

According to the comprehensive evaluation of the Q value in Table 1, the hyperchaotic attractor corresponding to $a = 1.2$ in Case 3 depicted in Fig. 12a3 and b3 has better dynamical performance than other hyperchaotic attractors and is worth further comparison and application. It is worth mentioning that the distribution of Q values in the $k_1 - k_2$ and $a - b$ parameter plane corresponds exactly to the dynamical distributions depicted in Figs. 5 and 6, which can be explained by the Q-value spectrum shown in Fig. 13. Specifically, under the inducement of adjustable parameters, as the periodic behavior switches to more complex hyperchaotic behavior, the Q values increase and approach yellow color, indicating an increase in the complexity of strange attractors. Consequently, the Q-value spectrum can reflect the dynamical performance of strange attractors, which is beneficial for exploring various high-performance hyperchaotic attractors.

4.2 Complexity enhancement of hyperchaotic sequences

To emphasize the complexity enhancement of the proposed HDM map, the comparisons and analyses of the dynamical performance indicators between the excellent hyperchaotic sequence corresponding to $a = 1.2$ in Case 3 and other chaotic/hyperchaotic sequences generated by multiple maps are performed. The maps used for comparisons are the MTM map [5], STB map [31], QDM map [32], Bao's map1 [33], Bao's map2 [33], Lai's map [38], NDMH map [39], Hénon map [40], and Lozi map [41]. At the same time, each map is set as the optimal parameters to ensure the fairness of the results, and comprehensive dynamical performance indicators are summarized in Table 2.

According to the indicators in Table 2, except for LE2, the hyperchaotic attractor generated by the proposed map exhibits the best dynamical performance, especially the values of LE1, PE, and CorDim. Specifically, compared with the QDM and NDMH maps constructed by only a single discrete memristor, the HDM map considering two discrete memristors can significantly promote the dynamical complexity. Particularly important is that the 3-D Bao's map1 and Bao's map2 are also constructed by two identical memristors, while the proposed HDM map is 2-D and contains two different memristors. However, the proposed map can generate more fascinating hyperchaotic sequences and enhance the complexity of
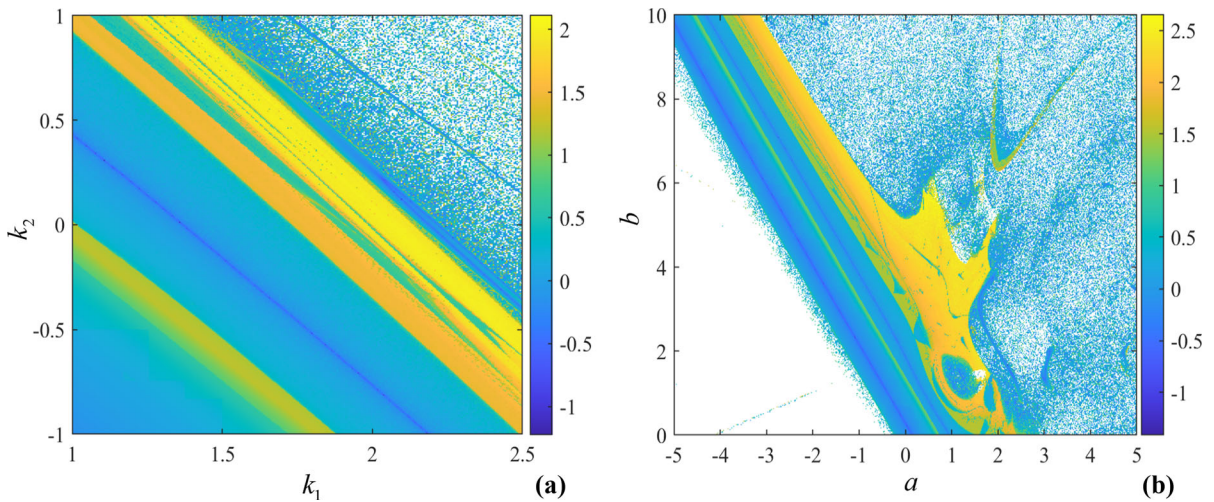
Fig. 13 Q-value spectrum shown on the 2-D parameter plane with $(x_0, q_0) = (0.1, 0.1)$. **a** For $(a, b) = (1, 1)$, $k_1 \in [1, 2.5]$ and $k_2 \in [-1, 1]$; **b** For $(k_1, k_2) = (1.5, 0.8)$, $a \in [-5, 5]$ and $b \in [0, 10]$

Table 2 Dynamical performance indicators of different maps

Maps	Parameters	LE1, LE2, LE3	SE	PE	SampE	IE	C0	CorDim	Q
Proposed map	(1.5, 0.8, 1.2, 4)	**0.5791, 0.0603**	**0.9333**	**5.3748**	**1.2147**	**7.9881**	**0.9738**	**2.6247**	**2.4686**
MTM map [5]	(− 0.6, 1.78)	0.3211, 0.1549	0.8686	4.1488	1.0870	7.9854	0.6795	1.7559	2.1251
STB map [31]	(1.9, 0.6)	0.3270, 0.0852	0.8087	3.8525	1.0517	7.9843	0.4675	1.7244	2.0377
QDM map [32]	1.78	0.2672, 0.0921	0.9226	3.4495	0.9503	7.9841	0.1781	1.6324	1.9345
Bao's map1 [33]	(0.86, 0.86)	0.1782, 0.1057, 0.0000	0.8854	3.6910	0.8734	7.9853	0.0913	1.6975	1.9385
Bao's map2 [33]	(0.9, 0.9)	0.2898, 0.0003, 0.0028	0.9257	2.4582	0.2369	7.9691	0.1466	0.9355	1.6203
Lai's map [38]	(− 0.1, 2.12, − 0.85, 0.1)	0.2908, 0.0514	0.7327	3.4494	0.9352	7.9870	0.3479	1.6093	1.9255
NDMH map [39]	(1.5,− 1,0.04,0.5,1.72,1)	0.1896, 0.0648	0.5585	3.7274	0.9357	7.9853	0.1761	2.1525	1.9739
Hénon map [40]	(1.4, 0.3)	0.4203, -1.6243	0.9319	3.6511	0.8838	7.9868	0.8382	1.2058	1.7867
Lozi map [41]	(1.7, 0.5)	0.4717,-1.1644	0.9124	3.8398	1.0182	7.9861	0.7701	1.3893	1.9028

Bao's map1 and Bao's map2 by the sinusoidal transformation in the case of lower dimension, which is of great significance and value. In addition, it can be seen from Table 2 that the complexity enhancement performance of the HDM map is more satisfactory than that of the STB map and Lai's map, which also use sinusoidal transformation. By coupling the discrete memristor and the traditional map, the MTM map can generate good hyperchaotic sequences, but its complexity is lower than that of the proposed map, which can be evaluated by the values of Q. Finally, two traditional maps can only generate chaotic attractors with one positive LE and one negative LE.

In contrast, the proposed map can generate two positive LEs, and the value of LE1 is the largest.

Ultimately, compared with the maps using different construction methods, the hyperchaotic sequence generated by the HDM map has the characteristics of complexity enhancement, which can be widely applied in chaos-based engineering fields, such as secure communication and image encryption.

4.3 Design and test of PRNGs

Hyperchaos is often applied to image encryption and other fields as the pseudo-random number (PRN), so

Table 3 NIST SP800-22 test results for two PRNGs

No.	Statistical tests	PRNG for Case3		PRNG for Case4	
		$P\text{-value}_T$ ≥ 0.0001	Pass rate ≥ 0.9628	$P\text{-value}_T$ ≥ 0.0001	Pass rate ≥ 0.9628
01	Frequency	0.4528	1.0000	0.1703	1.0000
02	Block Frequency	0.5009	0.9833	0.3505	1.0000
03	Cum. Sums (Forward)	0.6198	1.0000	0.6890	1.0000
	Cum. Sums (Backward)	0.2430	1.0000	0.6890	0.9917
04	Runs	0.7728	0.9833	0.8486	0.9833
05	Longest Run	0.6890	0.9917	0.9320	0.9833
06	Rank	0.2993	0.9833	0.1005	0.9917
07	FFT	0.0106	0.9917	0.5174	0.9833
08	Non-Ovla. Temp.*	0.4735	0.9899	0.5350	0.9912
09	Ovla. Temp	0.6890	1.0000	0.9705	0.9750
10	Universal	0.8195	1.0000	0.4220	0.9667
11	Appr. Entropy	0.1481	1.0000	0.9573	0.9917
12	Ran. Exc.*	0.3871	0.9941	0.4215	0.9863
13	Ran. Exc. Var.*	0.5275	0.9913	0.4960	0.9855
14	Serial(1st)	0.5009	0.9917	0.2873	0.9667
	Serial(2nd)	0.7565	1.0000	0.7887	0.9833
15	Linear Complexity	0.3242	0.9833	0.7399	1.0000
	Success Count	15/15	15/15	15/15	15/15

the design of PRNG and the randomness test of PRN are critical. Therefore, this section mainly studies the application performance of the HDM map in PRNG by the NIST SP800-22 suite.

Taking Case 3 and Case 4 as examples, two hyperchaotic sequences with superior dynamical performance are defined as $X_{Case3} = \{x(1), x(2), \cdots x(n), \cdots\}$ with $a = 1.2$ and $X_{Case4} = \{x(1), x(2), \cdots x(n), \cdots\}$ with $b = 5$. When each $x(n)$ in X_{Case3} and X_{Case4} is converted to a 52-bit binary stream $x_B(n)$ according to the IEEE 754 binary floating point number standard, by selecting the 37th to 44th bits in the mantissa of $x_B(n)$, two PRNGs can be constructed as

$$\begin{cases} P_{Case3}(i) = x_B(i)_{37:44}, \\ P_{Case4}(i) = x_B(i)_{37:44}. \end{cases} \tag{14}$$

Therefore, each PRNG in Eq. (14) can generate an 8-bit binary PRN related to the original hyperchaotic sequence in an iteration process. At this time, 120 sets of PRN test samples can be obtained through 14,999,999 iterations, and the sample length is 10^6. Finally, with the help of NIST SP800-22 containing 15 test items, a strict randomness test experiment is

performed, and the randomness of the PRNGs is measured according to the P value ($P - value_T$) and the pass rate. When $P - value_T \geq 0.0001$, PRN is uniformly distributed [42]. In addition, for PRNs with a sample size of 120, when the significance level is set to $\alpha = 0.01$, the minimum PRN pass rate can be calculated as 0.9628 by

$$\hat{p} \pm 3\sqrt{\frac{\hat{p}(1 - \hat{p})}{120}}, \tag{15}$$

where $\hat{p} = 1 - \alpha$. Therefore, the test results of PRNs generated by two PRNGs are counted in Table 3, where the subtest with an asterisk represents the average value. Since the corresponding $P - value_T$ and pass rate of PRNGs for Case3 and Case4 are greater than 0.0001 and 0.9628, respectively, it is demonstrated that the PRNs have passed the strict randomness test. In a word, PRNG tests show that hyperchaotic sequences generated by the HDM map have high randomness and application prospects.

4.4 Digital circuit experimental verification

It is well known that digital circuits play an important role in map-based engineering [5, 24]. To verify

various strange attractors presented in the numerical methods, especially the hyperchaotic attractors, it is essential to develop a digital circuit experimental platform for the HDM map. The proposed digital circuit experimental platform consists of a high-performance STM32F407ZGT6 development board with a 32-bit ARM Cortex-M4 processor, 168 MHz main frequency, 1024 KB embedded Flash and 192 KB embedded SRAM functions, a dual-channel 16-bit DAC8563 module for digital-to-analog conversion, a high-precision oscilloscope YOKOGAWA DL850E, and some peripheral circuits, as shown in Fig. 14. According to the HDM model (5) and the relevant parameters we are concerned with in Fig. 8, an iterative program based on C language is written and executed in the microcontroller to generate the corresponding digital signals. Subsequently, the digital signals corresponding to the state variables are converted into analog voltages through the DAC8563 module and accurately captured by the scopecorder. It is worth noting that the range of the two channels of the DAC8563 is specified as − 10 V to 10 V, and at the same time, it is decomposed into 2 V/div in the oscilloscope, so that the voltage values corresponding to each channel can be obtained directly.

Through the digital circuit implementations of the HDM map under different parameters, abundant and accurate experimental results are displayed in Fig. 15. By comparing the strange attractors depicted in Figs. 15 and 8, it clearly turns out that the developed microcontroller-based digital circuit platform for the HDM map can accurately reproduce the results of the numerical methods. That is to say, the effectiveness of the numerical results and the practicability of the HDM map are manifested.

5 Flexible switching control and application in image encryption

To promote the flexibility and verify the practical application value of the proposed map, this section mainly studies the flexible switching control of the HDM map and the application of the hyperchaotic sequence after switching control in image encryption.
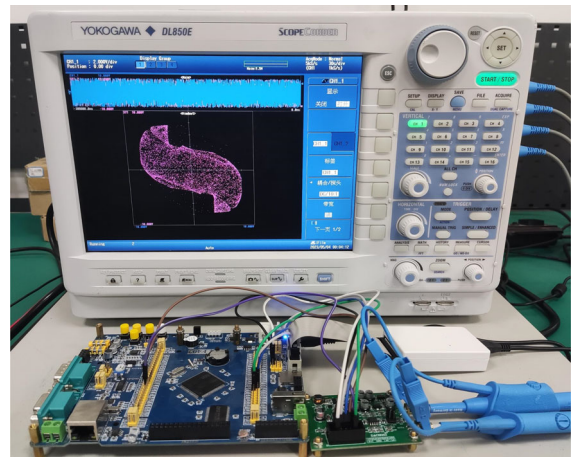

Fig. 14 A microcontroller-based digital circuit experimental platform for the HDM map

5.1 Flexible switching control of hyperchaotic sequences

In addition to complexity enhancement and randomness, the flexibility of hyperchaotic sequences cannot be ignored for practical engineering applications. Although some memristive discrete maps with sinusoidal or cosinusoidal memductance can achieve non-destructively offset-boosted switching, the flexibility is not high due to the lack of amplitude-controlled characteristics. Inspired by [35], the variable substitution is used to make the HDM map have both offset-boosted and amplitude-controlled characteristics. Assuming that the amplitude-controlled factors are α and β, and the offset-boosted factors are γ and δ, the flexible switching control of the HDM map can be realized after setting $x_n = \alpha \tilde{x}_n + \gamma$ and $q_n = \beta \tilde{q}_n + \delta$, where $\tilde{x}_n$ and $\tilde{q}_n$ are the switched sequences. Therefore, the HDM map can be transformed into

$$\begin{cases} \alpha \tilde{x}_{n+1} = k_1 \sin\left(\left((\beta \tilde{q}_n + \delta)^2 - a\right)(\alpha \tilde{x}_n + \gamma)\right) \\ \qquad + k_2 \sin((|\beta \tilde{q}_n + \delta| - b)(\alpha \tilde{x}_n + \gamma)) - \gamma, \\ \beta \tilde{q}_{n+1} = \beta \tilde{q}_n + \alpha \tilde{x}_n + \gamma. \end{cases} \quad (16)$$

For $(\beta, \gamma, \delta) = (1, 0, 0)$ and $(\alpha, \beta, \delta) = (1, 1, 0)$, taking the hyperchaotic sequence x corresponding to $a = 1.2$ in Case 3 as an example, according to Eq. (16), the amplitude-controlled characteristics related to α and the offset-boosted characteristics related to γ are depicted in Fig. 16. As shown in Fig. 16a1, as α increases, the amplitude of the iteration
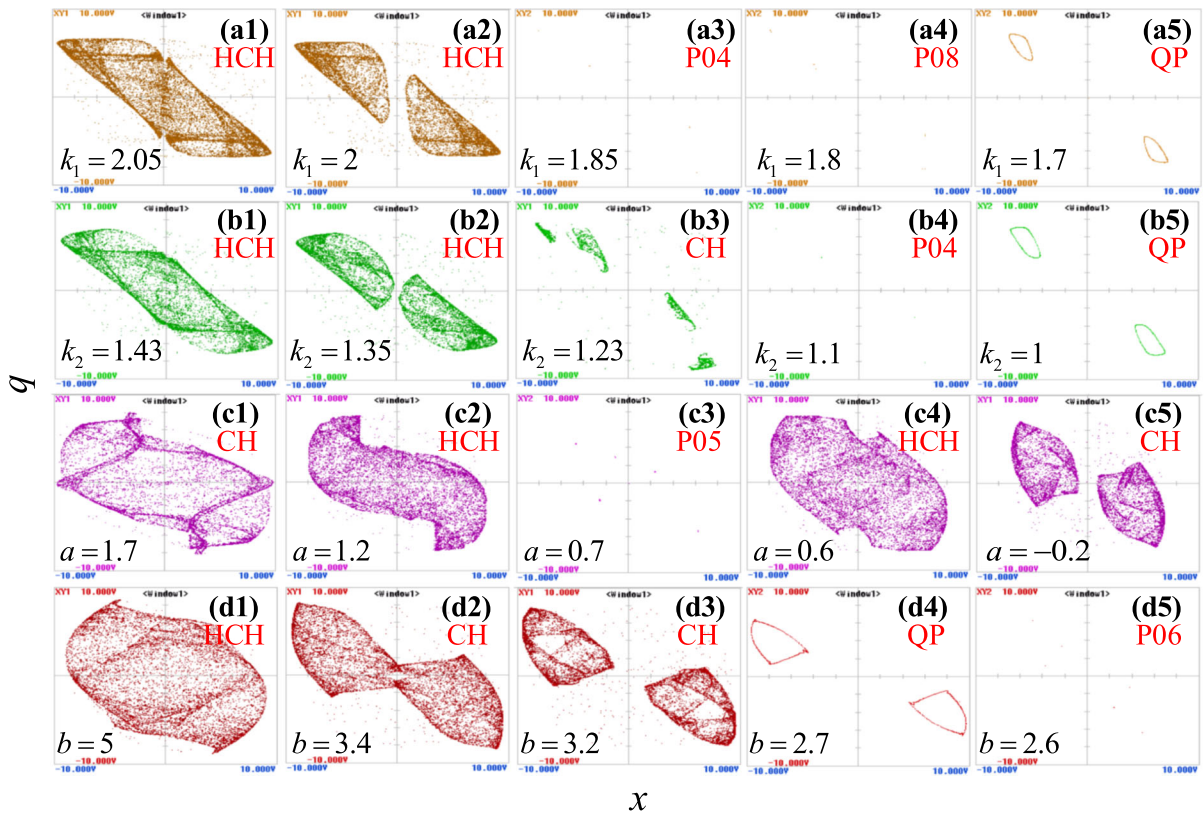
Fig. 15 Verification results of the microcontroller-based digital circuit platform for the HDM map with $(x_0, q_0) = (0.1, 0.1)$. **a** Case 1 with $k_1 = 2.05$, 2, 1.85, 1.8, and 1.7; **b** Case 2 with $k_2 = 1.43$, 1.35, 1.23, 1.1, and 1; **c** Case 3 with $a = 1.7$, 1.2, 0.7, 0.6, and -0.2; **d** Case 4 with $b = 5$, 3.4, 3.2, 2.7, and 2.6

sequence $\tilde{x}$ decreases proportionally, and the corresponding phase point on the $\tilde{x} - \tilde{q}$ plane in Fig. 16a2 shrinks along the x-axis, which demonstrates that α can control the amplitude of $\tilde{x}$ arbitrarily. However, as γ varies, since the hyperchaotic sequence $\tilde{x}$ and the phase points depicted in Fig. 16b1 and b2 are switched with offset fixed to 5 and the $\tilde{x}$ keeps the amplitude difference unchanged, the offset-boosted characteristics related to γ are verified. When the control parameters are set to $\alpha \in [1, 5]$ and $\gamma \in [-10, 10]$, respectively, the magenta bifurcation points in Fig. 16a3 and b3 display a shrinking and tilting trend, respectively, while that of the state $\tilde{q}$ depicted by the brown bifurcation points is not affected. That further indicates that flexible and independent switching control can be achieved by adjusting α and γ. It is emphasized that Fig. 16a4 and b4 reveals the influence mechanism of control factors on dynamical performance. Except for the slight change of the C0 value, other dynamical performance indicators show a

stable fluctuating straight line, indicating that the switching control hardly changes the incomparable dynamical performance of the original hyperchaotic sequences.

It should be noted that the flexible switching control for $\tilde{q}$ can be executed via β and δ, which can yield the same conclusions. Therefore, through switching control, the hyperchaos sequences generated by the HDM map have high flexibility and can be flexibly applied to various engineering fields without changing the dynamical performance.

5.2 Application in image encryption

Since the hyperchaotic sequence generated by the HDM map has high complexity, randomness, and flexibility, it can be used as a pseudo-random sequence to enhance the security of image encryption. This section proposes an image encryption scheme based
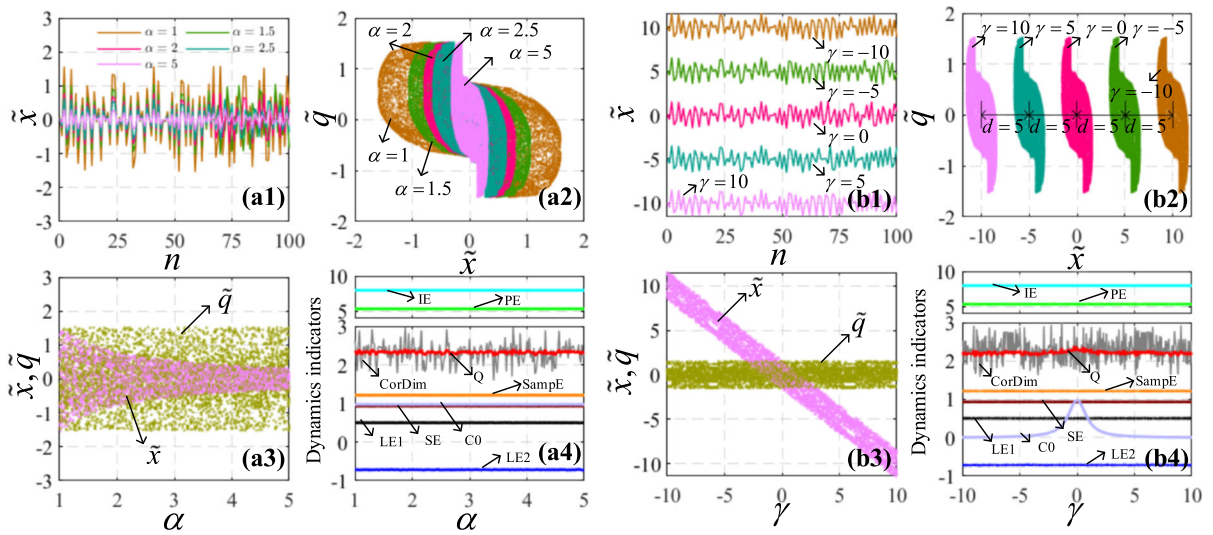
Fig. 16 Performance of flexible switching control for the HDM map. **(a1-a4)** For $(\beta, \gamma, \delta) = (1, 0, 0)$, the amplitude-controlled characteristics related to α; **(b1-b4)** For $(\alpha, \beta, \delta) = (1, 1, 0)$, the offset-boosted characteristics related to γ

on the HDM map, and the experimental results are discussed in detail.

5.2.1 Image encryption scheme design

Considering the lack of a diffusion process in [9, 10], a novel encryption strategy is introduced in detail, which mainly includes plain image input, hyperchaotic sequence generator, permutation, hybrid diffusion, substitution, and cipher image output processes, as shown in Fig. 17. Please note that the encryption process will be illustrated using the encryption of a color image as an example.

(1) Plain image input: Input a plain color image P with size $M \times N \times 3$, and decompose it into three pixel matrices of red P_R, green P_G, and blue P_B with size $M \times N$. Next, P_R is taken as a representative to illustrate the rest of the encryption process.

(2) Hyperchaotic sequence generator: Generate key sequences to encrypt the plain image P. By switching control based on the HDM map, the security of image encryption is enhanced because the control factors (α, β, γ and δ) enlarge the secret key space and can generate hyperchaotic key sequences with arbitrary amplitude and offset. Therefore, after $M \times N$ iterations, the hyperchaotic sequence generator can output three different pseudo-random key

sequences (K_1, K_2 and K_3), which are described as

$$\begin{cases} K_1 = x, \\ K_2 = \mathrm{mod}\big(floor\big(((x+q)/2) \times 10^{15}\big), 256\big), \\ K_3 = \mathrm{mod}\big(floor\big(x \times 10^{15}\big), 256\big), \end{cases}$$

$$(17)$$

where $\mathrm{mod}(x, 256)$ represents the remainder of x dividing by 256, while $floor(x)$ is the nearest integer less than or equal to x.

(3) Permutation: To reduce the correlation of pixels, P_R is converted into a row vector with size $1 \times L$, and permutated according to the index of K_1 in ascending order. The process is described as

$$P_R^1(1, j) = P_R(index(K_1(1, j))), \quad (18)$$

where $j = 1, 2, \ldots, L$ and $L = M \times N$.

(4) Hybrid diffusion: A hybrid diffusion scheme including forward, row-column association, and backward diffusions is designed and only needs to perform one round. If the diffused pixel matrices are defined as P_R^2, P_R^3 and P_R^4, respectively, the forward diffusion process is implemented by
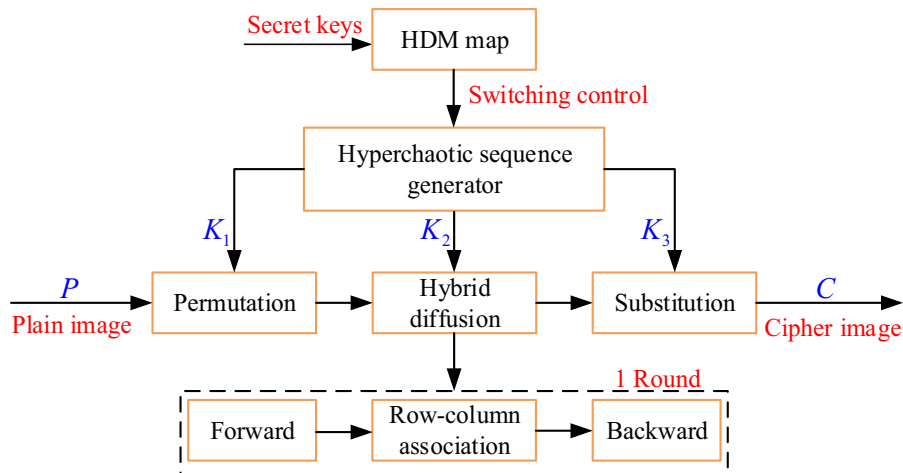
Fig. 17 Schematic diagram of the proposed image encryption scheme

$$\begin{cases} P_R^2(1,1) = \mathrm{mod}\left(P_R^1(1,1) + K_2(1), 256\right), \\ P_R^2(1,j) = \mathrm{mod}\left(P_R^2(1,j-1) + P_R^1(1,j) + K_2(j), 256\right), \end{cases} \tag{19}$$

where $j = 2, 3, \ldots, L$. In the row-column association diffusion process, the diffused pixel is the sum of the pixel values of adjacent rows, columns, and itself. At this time, P_R^2 is transformed into a matrix with size $M \times N$, then the process is described as

$$\begin{cases} P_R^3(1,1) = \mathrm{mod}\left(P_R^2(1,1) + P_R^2(1,N) + P_R^2(M,1), 256\right), \ i = j = 1; \\ P_R^3(i,1) = \mathrm{mod}\left(P_R^2(i,1) + P_R^3(i-1,1) + P_R^2(i,N), 256\right), \ i \geq 2; \\ P_R^3(1,j) = \mathrm{mod}\left(P_R^2(1,j) + P_R^3(1,j-1) + P_R^2(M,j), 256\right), \ j \geq 2; \\ P_R^3(i,j) = \mathrm{mod}\left(P_R^2(i,j) + P_R^3(i-1,1) + P_R^3(1,j-1), 256\right), \ i \geq 2 \text{ and } j \geq 2. \end{cases} \tag{20}$$

Similar to forward diffusion, converting P_R^3 to a row vector with size $1 \times L$, the backward diffusion process is expressed as

$$\begin{cases} P_R^4(1,L) = \mathrm{mod}\left(P_R^3(1,L) + K_2(L), 256\right), \\ P_R^4(1,j) = \mathrm{mod}\left(P_R^4(1,j+1) + P_R^3(1,j) + K_2(j), 256\right), \end{cases} \tag{21}$$

where $j = L-1, L-2, \ldots, 1$.

(5) Substitution: An XOR operation is used in this process, described as

$$P_R^5(1,j) = P_R^4(1,j) \oplus K_3(j), \tag{22}$$

where $j = 1, 2, \ldots, L$.

(6) Cipher image output: The final cipher image C can be obtained by reorganizing the encrypted

P_R^5, P_B^5, and P_C^5 into an image with size $M \times N \times 3$, and the corresponding decryption process is the reverse operation of the encryption process.

5.2.2 Experimental result analysis

To evaluate the performance of the encryption strategy, six different typical color plain images with size 512×512, named Lena, Peppers, Mandrill, Airplane, House, and Sailboat, are used for encryption experiments, as shown in Fig. 18. It is important to note that the typical test case images possess strong representativeness and ensure that the proposed encryption strategy performs well across a wide range of image categories, thereby increasing its generality and applicability. Additionally, these intentionally selected images have varying levels of complexity and features, which effectively test the robustness and reliability of the strategy. Notably, all these images are sourced from publicly available datasets [43], and the proposed encryption strategy has received widespread recognition in relevant fields for its effectiveness in encrypting these images. To comprehensively verify the effect of the encryption method, it is necessary to conduct encryption experiments in some non-typical test case images. Therefore, six non-typical grayscale images with different sizes are also considered, including Lung, Bird, and Moon Surface with a size of 256×256, and Brain, Bridge, and Fingerprint with a size of 512×512, as shown in Fig. 19. Firstly, the
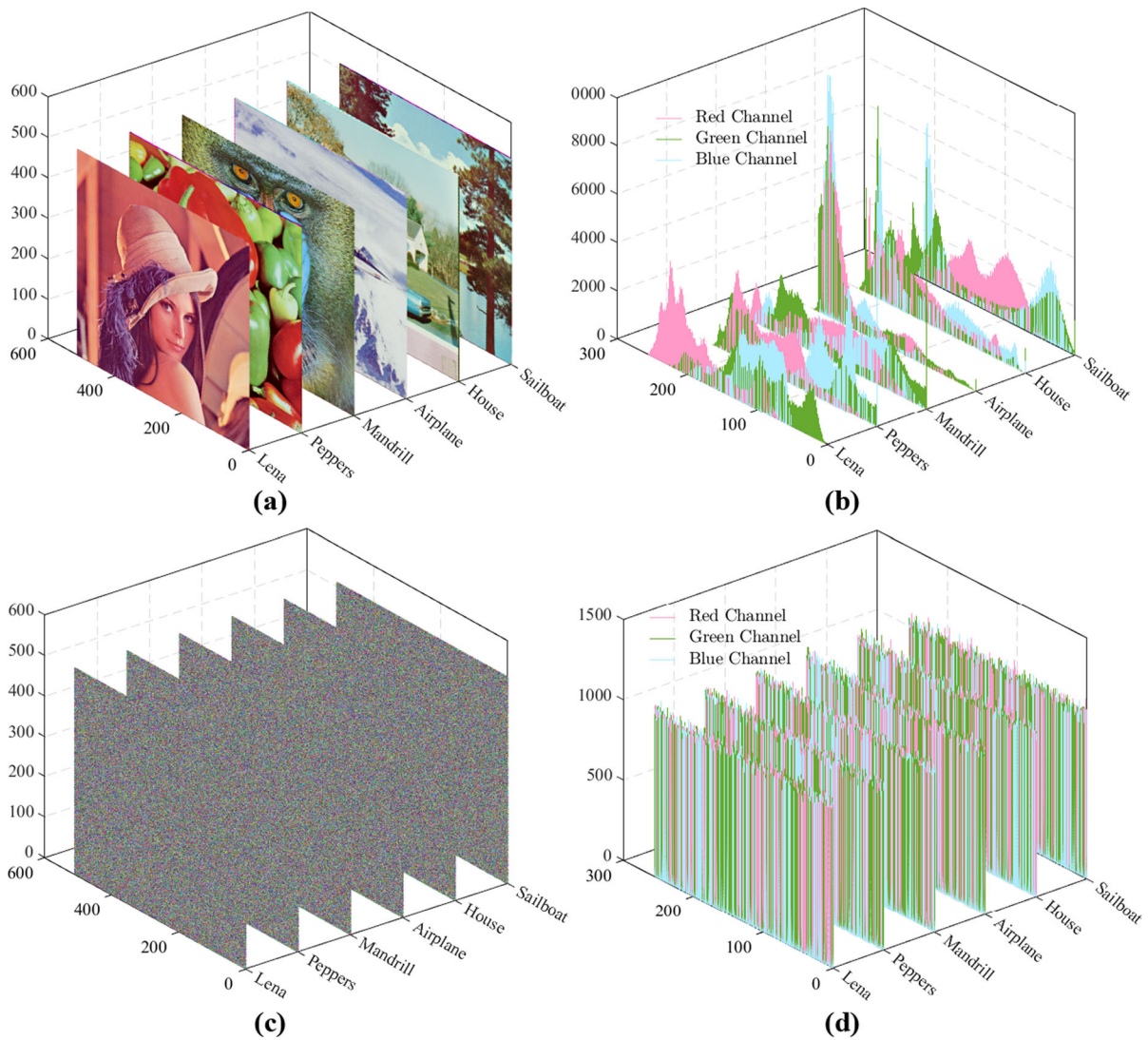
Fig. 18 Encryption results of six different typical color plain images. **a** Plain images; **b** Histogram of plain images; **c** Cipher images; **d** Histogram of cipher images

secret key is set to $(k_1, k_2, a, b, x_0, q_0, \alpha, \beta, \gamma, \delta) = (1.5, 0.8, 1.2, 4, 0.1, 0.1, 1.5, -1.5, 0.2, -0.2)$ and the key space can be calculated as $10^{15+16+15+15+17+16+15+15+16+16} = 10^{146} \approx 2^{485} \gg 2^{100}$ according to the key sensitivity analysis. Then, to display the effectiveness of the encryption strategy, the analyses of the histogram, pixel correlation, information entropy, differential attacks, data loss and noise attack are considered.

(1) Histogram analysis: The frequency of pixel values can be counted by the histogram, representing the distribution of image information.

The histogram of the six typical color plain images genuinely reflects the statistical characteristics of the pixel values in the red, green, and blue channels, as shown in Fig. 18b. However, the encrypted cipher images depicted in Fig. 18c present a chaotic and complex phenomenon, which effectively hides all the valuable information of the plain images. At the same time, Fig. 18d shows that the pixel values corresponding to the cipher images are uniformly distributed. In addition, for the non-typical grayscale images with different sizes and
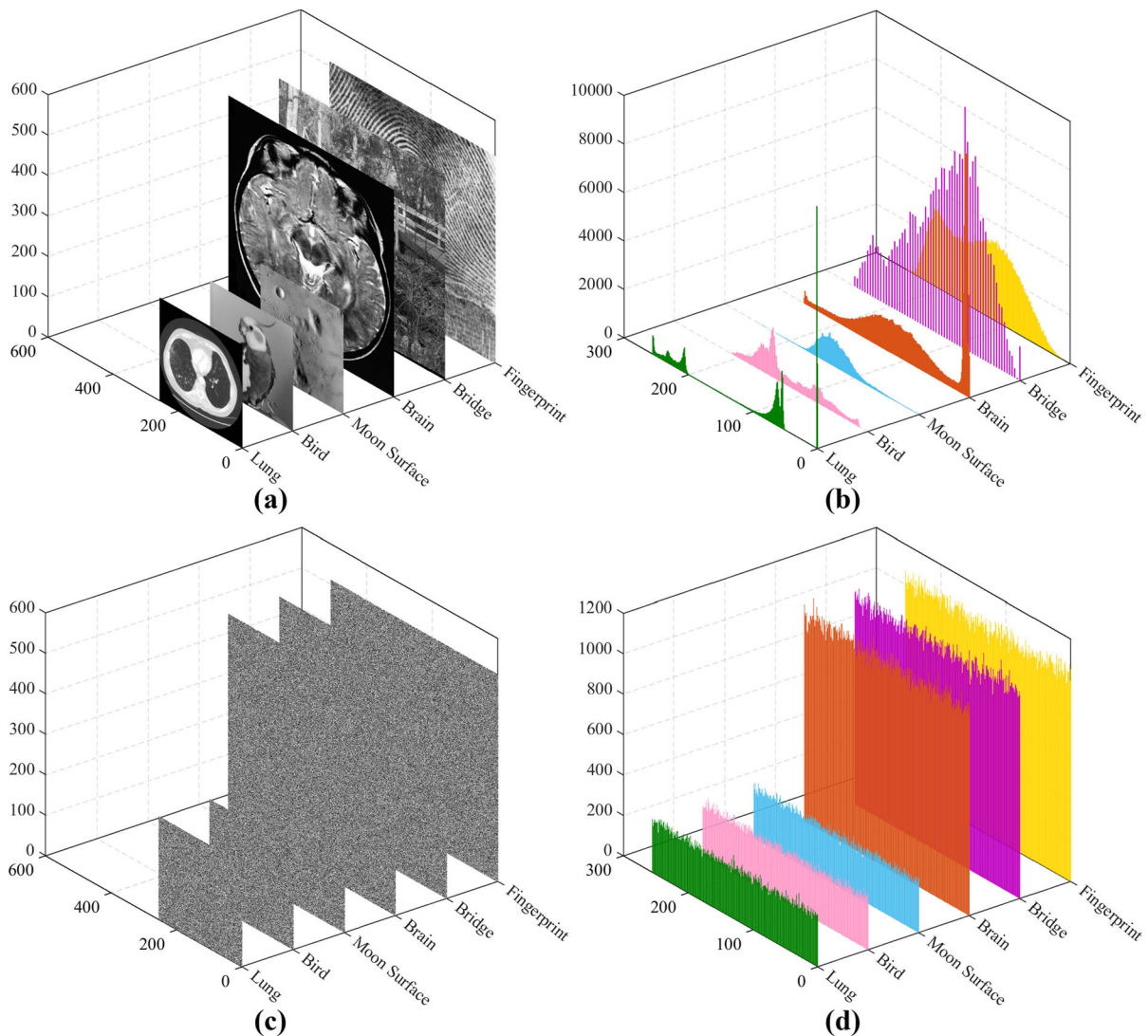
Fig. 19 Encryption results of six different non-typical grayscale plain images. **a** Plain images; **b** Histogram of plain images; **c** Cipher images; **d** Histogram of cipher images

categories given in Fig. 19a, the proposed encryption strategy can effectively change the distribution characteristics of the pixel values of the plain images in Fig. 19b and obtain the relatively stable pixel values displayed in Fig. 19d, indicating that the encryption strategy also has high applicability to non-typical images. Therefore, based on the difference between the plain images and the cipher images in Figs. 18 and 19, it is demonstrated that the proposed strategy can effectively encrypt the plain image and resist statistical attacks.

(2) Correlation analysis: The correlation between adjacent pixels is often measured by the correlation coefficient ρ_{xy} in the horizontal, vertical, and diagonal directions. When two adjacent pixel values are x and y, respectively, according to [44], ρ_{xy} can be expressed as

Table 4 Statistical results of correlation analysis for six typical images

Typical images	Plain images			Cipher images		
	Horizontal	Vertical	Diagonal	Horizontal	Vertical	Diagonal
Lena	0.96133	0.97626	0.94968	0.00301	0.00090	− 0.00070
Peppers	0.97018	0.97302	0.96057	− 0.00123	− 0.00073	0.00740
Mandrill	0.89579	0.83709	0.80959	− 0.00319	− 0.00167	0.00135
Airplane	0.96278	0.95071	0.92432	− 0.00184	− 0.00084	0.00210
House	0.95283	0.95664	0.91775	0.00444	0.00074	− 0.00036
Sailboat	0.96654	0.96288	0.94918	0.00061	− 0.00169	0.00394

Table 5 Statistical results of encryption performance for six non-typical grayscale plain images

Non-typical images	Size	Average correlation coefficient		Information entropy		NPCR	UACI
		Plain images	Cipher images	Plain images	Cipher images		
Lung	256×256	0.98105	0.00221	6.0762	7.9969	99.6111	33.4887
Bird	256×256	0.98027	0.00307	6.7744	7.9972	99.6145	33.4682
Moon Surface	256×256	0.91702	− 0.00131	6.7903	7.9974	99.6166	33.4629
Brain	512×512	0.97338	0.00028	6.9209	7.9993	99.6140	33.4657
Bridge	512×512	0.92136	0.00077	5.7056	7.9993	99.6035	33.4684
Fingerprint	512×512	0.90401	− 0.00047	6.7279	7.9994	99.6058	33.4746

$$\rho_{xy} = \frac{\sum\limits_{i=1}^{N}(x(i) - E(x))(y(i) - E(y))}{\sqrt{\sum\limits_{i=1}^{N}(x(i) - E(x))^2}\sqrt{\sum\limits_{i=1}^{N}(y(i) - E(y))^2}}, \quad (23)$$

where $E(x)$ and $E(y)$ are the average of the N pixel values $x(i)$ and $y(i)$. To evaluate the correlation of images, 20,000 pixel pairs are used, and the calculation results are summarized in Table 4. Please note that in the statistical results of encryption performance for six different non-typical grayscale plain images listed in Table 5, ρ_{xy} is calculated as the average of the correlation coefficients in the horizontal, vertical, and diagonal directions. It can be concluded that the ρ_{xy} of plain images is close to 1, while the ρ_{xy} of encrypted cipher images is close to 0, which shows that the correlation of plain images can be significantly reduced. Therefore, the proposed scheme can resist correlation attacks and strengthen the security of plain images.

Table 6 Statistical results of information entropy, NPCR, and UACI for six typical color cipher images

Images	Information entropy			NPCR	UACI
	R	G	B		
Lena	7.9994	7.9992	7.9994	99.6043	33.4668
Peppers	7.9992	7.9994	7.9993	99.6080	33.4652
Mandrill	7.9994	7.9992	7.9993	99.6152	33.4636
Airplane	7.9993	7.9992	7.9993	99.6096	33.4722
House	7.9992	7.9993	7.9993	99.6120	33.4793
Sailboat	7.9992	7.9992	7.9992	99.6058	33.4544

(3) Information entropy analysis: The useful information in the image can be measured by information entropy, and the greater the information entropy, the higher the degree of confusion and randomness of the image. A standard method for calculating information entropy can be expressed as

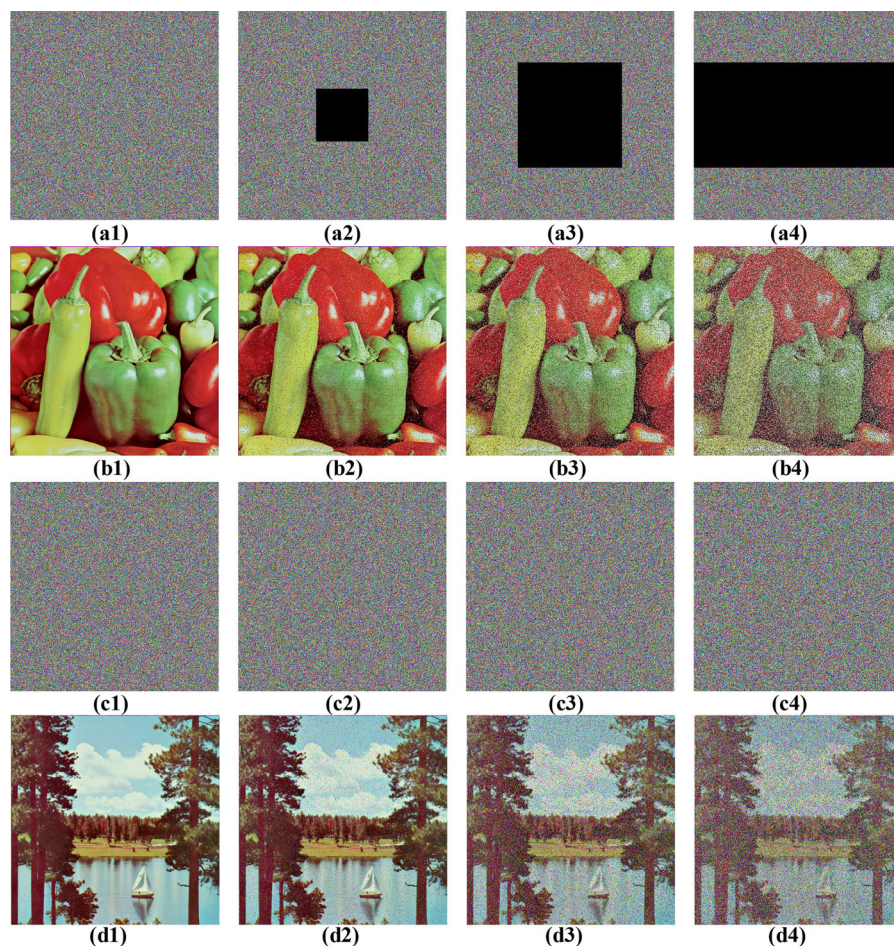$$H(x) = -\sum_{i=0}^{255} p(x_i) \log_2 p(x_i), \quad (24)$$

Fig. 20 Experimental data loss and noise attack analysis results for Peppers and Sailboat. **(a1, c1)** Cipher images; **(b1, d1)** Decrypted plain image; **(a2-a4)** Cipher images with 1/16, 1/4, and 1/2 data loss; **(b2-b4)** Decrypted plain images corresponding to (a2-a4); **(c2-c4)** Cipher images with 1%, 5%, and 10% salt and pepper noise; **(d2-d4)** Decrypted plain images corresponding to (c2-c4)

where $p(x_i)$ represents the probability of the pixel value x_i. For an encrypted image with high randomness due to $p(x_i) = 1/256$, the ideal information entropy is 8. Therefore, the information entropy of six typical color and six nontypical grayscale cipher images is listed in Tables 5 and 6, respectively. Since the values of the information entropy are all very close to 8, it is proved that the cipher images have high randomness, and the encryption strategy can effectively improve the security of plain images.

(4) Differential attack analysis: Since the differential attack on the cipher image may restore the plain image, the number of pixel change rate (NPCR) and the unified average changed

intensity (UACI) are commonly used to measure the ability of the encryption strategy to resist differential attacks. According to [45], the ideal NPCR and UACI are 99.6094% and 33.4635%, respectively. In order to obtain statistically significant results and increase credibility, 150 encryption experiments are performed by randomly adding 1 to a pixel of the typical and non-typical cipher images, and the average values of NPCR and UACI are shown in Tables 5 and 6. The statistical results show that the NPCR and UACI of all plain images are very close to the ideal value, which proves that the cipher image is susceptible to the small changes of the plain image, and the

encryption strategy can perfectly resist the differential attack.

(5) Data loss and noise attack analysis: It is essential to evaluate the decryption performance because the cipher image may be intercepted and interfered by noise. For this purpose, after cutting some data and adding noise to the cipher images, the decryption process is performed, and the robustness is analyzed. Figure 20a and b provides the decryption results of the Peppers cipher image for data loss, from which it can be observed that the decrypted Peppers plain image can clearly reflect the original information. When different intensities of salt and pepper noise are added to the Sailboat cipher image, the simulation results shown in Fig. 20c and d also highlight that the decryption process of the encryption scheme has good robustness. Therefore, the encryption strategy can effectively resist data loss and noise attacks.

From the above analysis, it can be concluded that the hyperchaotic key sequence generated by the HDM map shows high security performance and significant encryption effects in typical and non-typical image encryption. Therefore, the proposed HDM map can be further applied to secure communication.

6 Conclusions

The existing dual-memristor map has low complexity and flexibility, and the application value has not been verified. This paper has proposed a novel 2-D HDM mapping model with complexity enhancement through two different discrete memristors and sinusoidal transformation. The considered map has line invariant points related to coupling strengths, memristor initial condition, and parameters, while their stability is analyzed in detail. Strange attractors with multiple topological structures have been found in this map, such as periodic, quasi-periodic, chaotic, and hyperchaotic attractors. At the same time, the complex coexisting multi-stability is revealed through 3-D local basins of attraction, and the robust bi-stability dependent on initial conditions is further studied. In addition, the excellent dynamical performance of strange attractors, especially multiple hyperchaotic

attractors, is measured by comprehensive performance indicators. Importantly, by comparing with various maps, the complexity enhancement characteristic of the hyperchaotic sequence is strictly proved, and its high randomness is tested by PRNGs. In particular, the flexibility of the hyperchaotic sequence has been promoted by switching control, and the application value of the considered map that integrates all excellent performance is verified in image encryption. Specifically, the cipher images exhibit the uniformly distributed pixel values with extremely low correlation coefficients among them, as well as the information entropy close to 8, proving that the strategy can effectively enhance the security and randomness of the plain images. In terms of resistance to attacks, the NPCR and UACI values close to the ideal values demonstrate that the encryption strategy can effectively resist differential attacks. Under noise and data loss attacks, the original information of the cipher images can still be recovered, indicating that the strategy has strong robustness. Importantly, the encryption tests focus on typical color and non-typical grayscale images, providing strong support for the effectiveness and universality of the strategy. Finally, the developed microcontroller-based digital circuit platform accurately captures various strange attractors. In the future, it is worthwhile to construct dual-memristor mapping models with periodic memristances further to study the flexible switching control and extreme multi-stability.

Data availability Data will be made available on reasonable request.

Declarations

Conflict of interest The authors declare that there are no competing interests regarding the publication of this paper.

References

1. Chua, L.O.: Memristor-the missing circuit element. IEEE Trans. Circuit Theory. **18**, 507–519 (1971). https://doi.org/10.1109/TCT.1971.1083337

2. Strukov, D.B., Snider, G.S., Stewart, D.R., Williams, R.S.: The missing memristor found. Nature **453**, 80–83 (2008). https://doi.org/10.1038/nature06932

3. Zhang, S., Li, C., Zheng, J., Wang, X., Zeng, Z., Peng, X.: Generating any number of initial offset-boosted coexisting Chua's double-scroll attractors via piecewise-nonlinear memristor. IEEE Trans. Ind. Electron. **69**, 7202–7212 (2022). https://doi.org/10.1109/TIE.2021.3099231

4. Das, S.: Recurrence quantification and bifurcation analysis of electrical activity in resistive/memristive synapse coupled Fitzhugh-Nagumo type neurons. Chaos Solitons Fractals **165**, 112772 (2022). https://doi.org/10.1016/j.chaos.2022.112772

5. Li, H., Hua, Z., Bao, H., Zhu, L., Chen, M., Bao, B.: Two-dimensional memristive hyperchaotic maps and application in secure communication. IEEE Trans. Ind. Electron. **68**, 9931–9940 (2021). https://doi.org/10.1109/TIE.2020.3022539

6. Tong, Z., Nakane, R., Hirose, A., Tanaka, G.: A simple memristive circuit for pattern classification based on reservoir computing. Int. J. Bifurcation Chaos. **32**, 2250141 (2022). https://doi.org/10.1142/S0218127422501413

7. Njitacke, Z.T., Nkapkop, J.D.D., Signing, V.F., Tsafack, N., Sone, M.E., Awrejcewicz, J.: Novel extreme multi-stable tabu learning neuron: circuit implementation and application to cryptography. IEEE Trans. Ind. Inform. (2022). https://doi.org/10.1109/TII.2022.3223233

8. Lin, H., Wang, C., Sun, Y., Wang, T.: Generating n-scroll chaotic attractors from a memristor-based magnetized Hopfield neural network. IEEE Trans. Circuits Syst. II Express Briefs **70**, 311–315 (2023). https://doi.org/10.1109/TCSII.2022.3212394

9. Lin, H., Wang, C., Cui, L., Sun, Y., Zhang, X., Yao, W.: Hyperchaotic memristive ring neural network and application in medical image encryption. Nonlinear Dyn. **110**, 841–855 (2022). https://doi.org/10.1007/s11071-022-07630-0

10. Lin, H., Wang, C., Sun, J., Zhang, X., Sun, Y., Iu, H.H.C.: Memristor-coupled asymmetric neural networks: bionic modeling, chaotic dynamics analysis and encryption application. Chaos Solitons Fractals **166**, 112905 (2023). https://doi.org/10.1016/j.chaos.2022.112905

11. Ding, D., Chen, X., Yang, Z., Hu, Y., Wang, M., Niu, Y.: Dynamics of stimuli-based fractional-order memristor-coupled tabu learning two-neuron model and its engineering applications. Nonlinear Dyn. **111**, 1791–1817 (2023). https://doi.org/10.1007/s11071-022-07886-6

12. Li, S., Chen, G., Mou, X.: On the dynamical degradation of digital piecewise linear chaotic maps. Int. J. Bifurcation Chaos **15**, 3119–3151 (2005). https://doi.org/10.1142/S0218127405014052

13. Zheng, J., Hu, H., Xia, X.: Applications of symbolic dynamics in counteracting the dynamical degradation of digital chaos. Nonlinear Dyn. **94**, 1535–1546 (2018). https://doi.org/10.1007/s11071-018-4440-6

14. Hua, Z., Zhou, B., Zhou, Y.: Sine chaotification model for enhancing chaos and its hardware implementation. IEEE Trans. Ind. Electron. **66**, 1273–1284 (2019). https://doi.org/10.1109/TIE.2018.2833049

15. Sui, Y., Gao, H.: Modified echo state network for prediction of nonlinear chaotic time series. Nonlinear Dyn. **110**, 3581–3603 (2022). https://doi.org/10.1007/s11071-022-07788-7

16. Sangiorgio, M., Dercole, F.: Robustness of LSTM neural networks for multi-step forecasting of chaotic time series. Chaos Solitons Fractals **139**, 110045 (2020). https://doi.org/10.1016/j.chaos.2020.110045

17. Dudukcu, H.V., Taskiran, M., Cam Taskiran, Z.G., Yildirim, T.: Temporal Convolutional Networks with RNN approach for chaotic time series prediction. Appl. Soft Comput. **133**, 109945 (2023). https://doi.org/10.1016/j.asoc.2022.109945

18. Peng, Y., He, S., Sun, K.: A higher dimensional chaotic map with discrete memristor. AEU-Int. J. Electron. Commun. **129**, 153539 (2021). https://doi.org/10.1016/j.aeue.2020.153539

19. He, S., Sun, K., Peng, Y., Wang, L.: Modeling of discrete fracmemristor and its application. AIP Adv. **10**, 015332 (2020). https://doi.org/10.1063/1.5134981

20. Bao, B., Li, H., Wu, H., Zhang, X., Chen, M.: Hyperchaos in a second-order discrete memristor-based map model. Electron. Lett. **56**, 769–770 (2020). https://doi.org/10.1049/el.2020.1172

21. Peng, Y., Sun, K., He, S.: A discrete memristor model and its application in Hénon map. Chaos Solitons Fractals **137**, 109873 (2020). https://doi.org/10.1016/j.chaos.2020.109873

22. Adhikari, S.P., Sah, MPd., Kim, H., Chua, L.O.: Three fingerprints of memristor. IEEE Trans. Circuits Syst. I Regul. Pap. **60**, 3008–3021 (2013). https://doi.org/10.1109/TCSI.2013.2256171

23. Bao, B., Rong, K., Li, H., Li, K., Hua, Z., Zhang, X.: Memristor-coupled Logistic hyperchaotic map. IEEE Trans Circuits Syst. II Express Briefs. **68**, 2992–2996 (2021). https://doi.org/10.1109/TCSII.2021.3072393

24. Lai, Q., Yang, L., Liu, Y.: Design and realization of discrete memristive hyperchaotic map with application in image encryption. Chaos Solitons Fractals **165**, 112781 (2022). https://doi.org/10.1016/j.chaos.2022.112781

25. Wang, J., Gu, Y., Rong, K., Xu, Q., Zhang, X.: Memristor-based Lozi map with hidden hyperchaos. Mathematics **10**, 3426 (2022). https://doi.org/10.3390/math10193426

26. Li, C., Yang, Y., Yang, X., Lu, Y.: Application of discrete memristors in logistic map and Hindmarsh-Rose neuron. Eur. Phys. J. Spec. Top. **231**, 3209–3224 (2022). https://doi.org/10.1140/epjs/s11734-022-00645-z

27. Rong, K., Bao, H., Li, H., Hua, Z., Bao, B.: Memristive Hénon map with hidden Neimark-Sacker bifurcations. Nonlinear Dyn. **108**, 4459–4470 (2022). https://doi.org/10.1007/s11071-022-07380-z

28. Bao, H., Hua, Z., Li, H., Chen, M., Bao, B.: Memristor-based hyperchaotic maps and application in auxiliary classifier generative adversarial nets. IEEE Trans. Ind. Inform. **18**, 5297–5306 (2022). https://doi.org/10.1109/TII.2021.3119387

29. Li, H., Li, C., Du, J.: Discretized locally active memristor and application in logarithmic map. Nonlinear Dyn. **111**, 2895–2915 (2023). https://doi.org/10.1007/s11071-022-07955-w

30. Deng, Y., Li, Y.: Nonparametric bifurcation mechanism in 2-D hyperchaotic discrete memristor-based map. Nonlinear Dyn. **104**, 4601–4614 (2021). https://doi.org/10.1007/s11071-021-06544-7

31. Bao, H., Li, H., Hua, Z., Xu, Q., Bao, B.: Sine-transform-based memristive hyperchaotic model with hardware implementation. IEEE Trans. Ind. Inf. **19**, 2792–2801 (2023). https://doi.org/10.1109/TII.2022.3157296

32. Bao, H., Hua, Z., Li, H., Chen, M., Bao, B.: Discrete memristor hyperchaotic maps. IEEE Trans. Circuits Syst. I Regul. Pap. **68**, 4534–4544 (2021). https://doi.org/10.1109/TCSI.2021.3082895

33. Bao, H., Gu, Y., Xu, Q., Zhang, X., Bao, B.: Parallel bi-memristor hyperchaotic map with extreme multistability. Chaos Solitons Fractals **160**, 112273 (2022). https://doi.org/10.1016/j.chaos.2022.112273

34. Yuan, F., Xing, G., Deng, Y.: Flexible cascade and parallel operations of discrete memristor. Chaos Solitons Fractals **166**, 112888 (2023). https://doi.org/10.1016/j.chaos.2022.112888

35. Kong, S., Li, C., He, S., Çiçek, S., Lai, Q.: A memristive map with coexisting chaos and hyperchaos. Chin. Phys. B. **30**, 110502 (2021). https://doi.org/10.1088/1674-1056/abf4fb

36. Sayama, H.: Introduction to the modeling and analysis of complex systems. Open SUNY Textbooks, Geneseo (2015)

37. Von Bremen, H.F., Udwadia, F.E., Proskurowski, W.: An efficient QR based method for the computation of Lyapunov exponents. Phys. D **101**, 1–16 (1997). https://doi.org/10.1016/S0167-2789(96)00216-3

38. Lai, Q., Lai, C.: Design and implementation of a new hyperchaotic memristive map. IEEE Trans. Circuits Syst. II Express Briefs **69**, 2331–2335 (2022)

39. Deng, Y., Li, Y.: Bifurcation and bursting oscillations in 2D non-autonomous discrete memristor-based hyperchaotic map. Chaos Solitons Fractals **150**, 111064 (2021). https://doi.org/10.1016/j.chaos.2021.111064

40. Henon, M.: A two-dimensional mapping with a strange attractor. Commun. Math. Phys. **50**, 69–77 (1976)

41. Botella-Soler, V., Castelo, J.M., Oteo, J.A., Ros, J.: Bifurcations in the Lozi map. J. Phys. Math. Theor. **44**, 305101 (2011). https://doi.org/10.1088/1751-8113/44/30/305101

42. Rukhin, A., Soto, J., Nechvatal, J., Barker, E., Leigh, S., Levenson, M., Banks, D., Heckert, A., Dray, J.: A statistical test suite for random and pseudorandom number generators for cryptographic applications. National Institute of Standards and Technology, Gaithersburg, MD, USA (2010)

43. USC-SIPI image database. https://sipi.usc.edu/database/. Accessed 3 May 2023

44. Lai, Q., Hu, G., Erkan, U., Toktas, A.: High-efficiency medical image encryption method based on 2D Logistic-Gaussian hyperchaotic map. Appl. Math. Comput. **442**, 127738 (2023). https://doi.org/10.1016/j.amc.2022.127738

45. Hua, Z., Zhou, Y.: Image encryption using 2D Logistic-adjusted-Sine map. Inf. Sci. **339**, 237–253 (2016). https://doi.org/10.1016/j.ins.2016.01.017